Syntheses, NMR and EPR Spectroscopy, Electrochemical Properties, and Structural Studies of [5,10,15,20-Tetrakis(perfluoroalkyl)porphinato]iron(II) and -iron(III) Complexes

Kevin T. Moore, James T. Fletcher, and Michael J. Therien*

Contribution from the Department of Chemistry, University of Pennsylvania, Philadelphia, Pennsylvania 19104-6323

Received May 14, 1998

Abstract: Syntheses, structural studies, electrochemistry, and spectroscopy of a number of [5,10,15,20-tetrakis-(heptafluoropropyl)porphinato]iron derivatives are presented. The X-ray crystal structure of 5,10,15,20-tetrakis-(heptafluoropropyl)porphinato]iron(II)·(pyridine)$_2$ exhibits a substantial S_4 distortion of the porphyrin macrocycle, with the *meso*-carbon atoms displaced more than 0.6 Å above and below the porphyrin mean plane defined by the four central nitrogen atoms; the most notable aspect of this ferrous porphyrin structure is the fact that it exhibits metrical features commonly manifested in crystallographically characterized ferric porphyrin complexes. X-ray data are as follows: $P2_1/n$ with $a = 12.772(1)$ Å, $b = 18.895(2)$ Å, $c = 19.756(2)$ Å, $\beta = 99.960(6)°$, $V = 4695.7(8)$ Å^3, $Z = 4$, and $d_{calc} = 1.689$ g/cm^3. ^{19}F NMR spectroscopy confirms the sensitivity of the ^{19}F nucleus as a probe of macrocycle aromaticity and electronic structure, while ^{1}H NMR spectroscopic studies show large isotropic shifts for the β-protons of the (porphinato)iron(III) chloride derivative ($\delta = 101.5$ and 86.4 ppm). Electrochemical data obtained from cyclic voltammetric and spectroelectrochemical experiments reveal that the $E_{1/2}$ value for the $Fe^{II/III}$ redox couple for 5,10,15,20-tetrakis(heptafluoropropyl)porphinato]-iron·(pyridine)$_2$ is shifted by 550 mV relative to that observed for the corresponding (porphinato)iron(III) chloride complex. The cathodic electrochemistry of [5,10,15,20-tetrakis(heptafuoropropyl)porphinato]iron·(pyridine)$_2$ is also unusual in that the first one-electron reduction of this complex produces a largely macrocycle-localized radical anion. EPR spectroscopic data shows that 5,10,15,20-tetrakis(heptafluoropropyl)porphinato]-iron(III)·(pyridine)$_2$ manifests a pure axial spectrum ($\Delta/\lambda = -26.4$; $\Sigma g^2 = 12.53$) congruent with a $(d_{xz},d_{yz})^4(d_{xy})^1$ electronic ground state. The extraordinary structural, potentiometric, and spectroscopic properties of these (porphinato)iron species arise from substantially reduced metal-centered electron density effected by the macrocycle's non-π-conjugating, σ-electron-withdrawing *meso*-perfluoroalkyl substituents.

Introduction

5,10,15,20-Tetrakis(perfluoroalkyl)porphyrins[1−3] [$(R_f)_4PH_2$] constitute a new class of highly electron-deficient macrocycles that differ markedly from the extensively studied 2,3,7,8,12,-13,17,18-octahalo-5,10,15,20-tetrakis(pentafluorophenyl)porphyrin [X_8TFPPH_2] ligand systems.[4] For example, X-ray photoelectron spectroscopic and cyclic voltammetric studies carried out on [$(R_f)_4PH_2$] and their (porphinato)zinc(II) [$(R_f)_4$-PZn] derivatives demonstrate that these species exhibit considerably reduced electron density in the porphyrin π system, as well as significantly augmented electrostatic potential at the nitrogen core orbitals.[1a,b] The lack of heavy atom substituents at the macrocycle periphery coupled with the fact that the non-π-conjugating, σ-electron-withdrawing perfluoroalkyl moieties stabilize the porphyrin HOMO and LUMO to the same degree endow these species with novel photophysical properties.[1b] Such physical and spectroscopic characteristics, coupled with their ease of synthesis and readily tailored solubility properties, place these compounds in a class by themselves with respect to all other porphyrin and (porphinato)zinc(II) species studied to date.[1,2]

In this report, we further elaborate the transition-metal

(1) (a) DiMagno, S. G.; Williams, R. A.; Therien, M. J. *J. Org. Chem.* **1994**, *59*, 6943−6948. (b) Goll, J. G.; Moore, K. T.; Ghosh, A.; Therien, M. J. *J. Am. Chem. Soc.* **1996**, *118*, 8344−8354. (c) Moore, K. T.; Horváth, I. T.; Therien, M. J. *J. Am. Chem. Soc.* **1997**, *119*, 1791−1792. (d) Moore, K. T.; Horváth, I. T.; Therien, M. J. *J. Am. Chem. Soc.*, manuscript submitted for publication.

(2) (a) DiMagno, S. G.; Wertsching, A. K.; Ross, C. R., II *J. Am. Chem. Soc.* **1995**, *117*, 8279−8280. (b) DiMagno, S. G.; Dussault, P. H.; Schultz, J. A. *J. Am. Chem. Soc.* **1996**, *118*, 5312−5313. (c) Woller, E. K.; DiMagno, S. G. *J. Org. Chem.* **1997**, *62*, 1588−1593.

(3) Wijesekera, T. P.; Lyons, J. E.; Ellis, P. E., Jr. *Catal. Lett.* **1995**, *36*, 69−73.

(4) (a) Traylor, T. G.; Tsuchiya, S. *Inorg. Chem.* **1987**, *26*, 1338−1339. (b) Hoffmann, P.; Labat, G.; Robert, A.; Meunier, B. *Tetrahedron Lett.* **1990**, *31*, 1991−1994. (c) Bartoli, J. F.; Brigaud, O.; Battioni, P.; Mansuy, D. *J. Chem. Soc., Chem. Commun.* **1991**, 440−442. (d) Campestrini, S.; Robert, A.; Meunier, B. *J. Org. Chem.* **1991**, *56*, 3725−3727. (e) Battioni, P.; Brigaud, O.; Desvaux, H.; Mansuy, D.; Traylor, T. G. *Tetrahedron Lett.* **1991**, *32*, 2893−2896. (f) Traylor, T. G.; Hill, K. W.; Fann, W.-P.; Tsuchiya, S.; Dunlap, B. E. *J. Am. Chem. Soc.* **1992**, *114*, 1308−1312. (g) Hoffmann, P.; Meunier, B. *New J. Chem.* **1992**, *16*, 559−561. (h) Lyons, J. E.; Ellis, P. E., Jr. *Appl. Catal. A* **1992**, *84*, L1−L6. (i) Banfi, S.; Mandelli, R.; Montanari, F.; Quici, S. *Gazz. Chim. Ital.* **1993**, *123*, 409−415. (j) Sorokin, A.; Robert, A.; Meunier, B. *J. Am. Chem. Soc.* **1993**, *115*, 7293−7299. (k) Lyons, J. E.; Ellis, P. E., Jr.; Myers, H. K., Jr.; Wagner, R. W. *J. Catal.* **1993**, *141*, 311−315. (l) Grinstaff, M. W.; Hill, M. G.; Labinger, J. A.; Gray, H. B. *Science* **1994**, *264*, 1311−1313. (m) Labinger, J. A. *Catal. Lett.* **1994**, *26*, 95−99. (n) Pattou, D.; Labat, G.; Defrance, S.; Séris, J.-L.; Meunier, B. *Bull. Soc. Chim. Fr.* **1994**, *131*, 78−88. (o) Lyons, J. E.; Ellis, P. E., Jr.; Myers, H. K., Jr. *J. Catal.* **1995**, *155*, 59−73.

10.1021/ja9816741 CCC: $18.00
Published on Web 05/20/1999

chemistry of the $(R_f)_4PH_2$ ligand system, and describe the syntheses, nuclear magnetic resonance spectroscopy, electrochemical properties, electronic absorption features, electron paramagnetic resonance spectroscopy, and structural characteristics of [5,10,15,20-tetrakis(heptafluoropropyl)porphinato]iron [$(C_3F_7)_4$PFe] derivatives and compare them to other benchmark (porphinato)iron (PFe) systems. These studies reveal that the $(R_f)_4PH_2$ ligand framework endows the ferric and ferrous oxidation states with electronic features distinct from those observed in all other PFe complexes examined to date.

Experimental Section

Materials. Inert atmosphere manipulations and solvent purification were carried out as described previously.[5] [5,10,15,20-Tetrakis(pentafluorophenyl)-2,3,7,8,12,13,17,18-octabromoporphinato]iron(III)·chloride, [5,10,15,20-tetrakis(pentafluorophenyl)porphinato]iron(III)·chloride, and 5,10,15,20-(tetraphenylporphinato)iron(III) chloride were synthesized according to literature methods.[4,6,7] Chemical shifts for ^{1}H NMR spectra are relative to residual protium in the deuterated solvents ($CDCl_3$, $\delta = 7.24$ ppm), while those for ^{19}F NMR spectra are referenced to fluorotrichloromethane ($CFCl_3$, $\delta = 0.00$ ppm). Chromatographic purification of all newly synthesized compounds was accomplished on the benchtop using neutral alumina (Fisher Scientific, Brockmann activity I, 200 mesh); because the electron-deficient porphyrin macrocycles utilized in this study stabilize the ferrous oxidation state, isolation of their respective (porphinato)iron·(pyridine)$_2$ complexes could be accomplished in an aerobic environment. The supporting electrolyte used in the electrochemical experiments, tetra-*n*-butylammonium perchlorate, was obtained from Alfa Aesar Johnson Matthey. Elemental analyses were performed by Robertson Microlit Laboratories, Inc (Madison, NJ). Mass spectra were performed at the Mass Spectrometry Center at the University of Pennsylvania.

Instrumentation. Electronic spectra were recorded on an OLIS UV/vis/NIR spectrophotometry system that is based on the optics of a Cary 14 spectrophotometer. NMR spectra were recorded on either a 200 MHz AM-200 or 250 MHz AC-250 Bruker spectrometer. Cyclic voltammetric and spectroelectrochemical experiments were performed with an EG&G Princeton Applied Research model 273A potentiostat/galvanostat. The cyclic voltammetric experiments utilized a single-compartment electrochemical cell with either a platinum or glassy carbon working electrode. Potential-dependent electronic absorption spectral experiments utilized an optically transparent platinum gauze working electrode in a nitrogen-sealed thin-layer spectroelectrochemical cell; the cell design has been described in detail elsewhere.[8]

[5,10,15,20-Tetrakis(heptafluoropropyl)porphinato]iron(II)·(Pyridine)$_2$. 5,10,15,20-Tetrakis(heptafluoropropyl)porphyrin [$(C_3F_7)_4PH_2$] was synthesized and purified by methods previously described.[1] The $(C_3F_7)_4PH_2$ ligand (100 mg, 0.102 mmol), and ferrous chloride tetrahydrate (350 mg, 1.76 mmol) were dissolved in dry, degassed pyridine (25 mL) and refluxed for 10 h under a N_2 atmosphere in a 100-mL Schlenk flask equipped with a condenser. Following evaporation of the solvent, the PFe complex was purified by flash chromatography on neutral alumina using 9:1 CH_2Cl_2:pyridine. The first red band was collected; removal of the solvents in vacuo gave a reddish solid, which was recrystallized from hot hexanes to yield analytically pure rectangular crystals. Isolated yield = 105 mg (86.4% based on 100 mg of $(C_3F_7)_4PH_2$). ^{1}H NMR (250 MHz, $CDCl_3$) δ 9.03 (s, 8H), 5.95 (d, 4H), 4.97 (t, 2H), 2.09 (d, 4H). ^{19}F NMR (200 MHz, $CDCl_3$) δ −79.97 (s, 12F), −86.21 (b, 8F), −119.37 (bs, 8F). UV−vis (CH_2Cl_2), [λ_{max} (nm), log ϵ (M^{-1} cm^{-1})] 340 (4.47), 418 (4.95), 542 (3.76), 575 (4.28). Anal. Calcd for $C_{42}H_{18}N_6F_{28}Fe$: C, 42.23; H, 1.52; N, 7.04. Found: C, 42.21; H, 1.51; N, 7.43.

{[5,10,15,20-Tetrakis(heptafluoropropyl)porphinato]iron-(III)}$_2$O. The $(C_3F_7)_4PH_2$ ligand (100 mg, 0.102 mmol) was dissolved in dry THF (25 mL) in a 100-mL Schlenk flask under an atmosphere of N_2. Lithium bis(trimethylsilyl)amide was added as a solid (35 mg, 0.210 mmol); the color immediately changed from deep purple to green upon formation of $(C_3F_7)_4PLi_2\cdot(THF)_2$.[9] The solution was stirred for an additional h, and anhydrous $FeCl_2$ (250 mg, 1.16 mmol) was added. The color of the reaction mixture gradually changed from green to brilliant red over a 3-h period; the Schlenk flask was then opened to air, giving rise to a deep olive green solution. After the volatiles were evaporated, the solid material was dissolved in CH_2Cl_2 and loaded on a neutral alumina column. Traces of free base porphyrin were first eluted with methylene chloride; the PFe complex was eluted with THF. After removal of solvent, the green (porphinato)iron(III) product was partitioned with CH_2Cl_2 and 3 M aqueous NaOH to ensure complete formation of the $[(C_3F_7)_4PFe]_2O$ complex. Isolated yield = 90 mg (84.6% based on 100 mg of $(C_3F_7)_4PH_2$). ^{1}H NMR (250 MHz, $CDCl_3$) δ 13.2 (s, 8H). ^{19}F NMR (200 MHz, $CDCl_3$) δ −73.12 (bs, 8F), −77.18 (bs, 12F), −119.60 (bs, 8F). UV−vis (CH_2Cl_2): 373 (4.17), 422 (4.12), 571 (3.32), 603 (3.54). Laser Desorption MS (M^+): 2087 (calcd 2087).

[5,10,15,20-Tetrakis(heptafluoropropyl)porphinato]iron(III)·Chloride. To a stirring solution of $[(C_3F_7)_4PFe]_2O$ (100 mg, 0.051 mmol) in CH_2Cl_2 (25 mL), an equal volume of 3 M aqueous HCl was added. A color change from olive green to deep purple immediately ensued; the mixture was further stirred for 1 h, after which time the organic layer was collected, washed with water, dried over $CaCl_2$, and evaporated. Isolated yield = 95 mg (92.9% based on 100 mg $[(C_3F_7)_4PFe]_2O$). ^{1}H NMR (250 MHz, $CDCl_3$) δ 101.7 (b, 4H), 86.4 (b, 4H). ^{19}F NMR (200 MHz, $CDCl_3$) δ 75.46 (b, 4F), 51.76 (b, 4F), −73.75 (b, 12 F), −80.17 (b, 8F). UV−vis (CH_2Cl_2): 350 (4.44), 405 (4.51), 507 (3.71), 647 (3.47). FAB MS (M^+ − axial Cl) 1036 (calcd 1036).

Spectroelectrochemical Experiments. The spectroelectrochemical cell utilized an optically transparent working electrode constructed from Pt gauze (Alfa Aesar, 0.1-mm diameter wire, 52 mesh), a SCE reference electrode, and a Pt wire counter electrode. The electrolyte solution consisted of 0.5 M tetra-*n*-butylammonium perchlorate (TBAP) in CH_2Cl_2. The analyte concentration in these experiments was 0.14 mM for [5,10,15,20-tetrakis(heptafluoropropyl)porphinato]iron(II)·(pyridine)$_2$ and 0.40 mM for [5,10,15,20-tetrakis(heptafluoropropyl)porphinato]iron-(III)·chloride. Potentials were stepped in 50-mV increments; electronic spectra were taken at 5-min intervals, which exceeded the time required for the current passed at the working electrode to cease.

X-ray Crystallography. The crystal structure for [5,10,15,20-tetrakis(heptafluoropropyl)porphinato]iron(II)·(pyridine)$_2$ was solved by direct methods (SIR88).[10] Table 1 contains details of the crystal and data collection parameters. The structure was determined by Dr. Patrick Carroll at the X-ray facility at the Department of Chemistry, University of Pennsylvania.

Crystallization of [5,10,15,20-Tetrakis(heptafluoropropyl)porphinato]iron(II)·(Pyridine)$_2$. X-ray quality crystals were obtained by cooling a saturated hexane solution of [5,10,15,20-tetrakis(heptafluoropropyl)porphinato]iron(II)·(pyridine)$_2$; translucent, rectangular crystals formed over a 48-h period. The crystal dimensions were 0.35 × 0.30 × 0.15 mm. The bis(pyridyl) adduct of [5,10,15,20-tetrakis(heptafluoropropyl)porphinato]iron(II) crystallizes in the monoclinic space group $P2_1/n$ with $a = 12.772(1)$ Å, $b = 18.895(2)$ Å, $c = 19.756(2)$ Å, $\beta = 99.960(6)°$, $V = 4695.7(8)$ Å^3, $Z = 4$, and $d_{calc} = 1.689$ g/cm^3. X-ray intensity data were collected on an MSC/RAXIS IIc area detector employing graphite-monochromated Mo Kα radiation ($\lambda = 0.7107$ Å) at 235 K. A total of 29 068 reflections were measured over the ranges: $4 \le 2\theta \le 50°$, $-15 \le h \le 15$, $-22 \le k \le 22$, $-23 \le l \le 23$.

The intensity data were corrected for Lorentz and polarization effects but not for absorption. Of the reflections measured, a total of 5097

(5) DiMagno, S. G.; Lin, V. S.-Y.; Therien, M. J. *J. Org. Chem.* **1993**, *58*, 5983−5993.

(6) (a) Lyons, J. E.; Ellis, P. E., Jr. *Catal. Lett.* **1991**, *8*, 45−51. (b) Bhyrappa, P.; Krishnan, V. *Inorg. Chem.* **1991**, *30*, 239−245. (c) Mandon, D.; Ochsenbein, P.; Fischer, J.; Weiss, R.; Jayaraj, K. Austin, R. N.; Gold, A.; White, P. S.; Brigaud, O.; Battioni, P.; Mansuy, D. *Inorg. Chem.* **1992**, *31*, 2044−2049.

(7) (a) Adler, A. D.; Sklar, L.; Longo, F. R.; Finarelli, J. D.; Finarelli, M. G. *J. Heterocycl. Chem.* **1968**, *5*, 669−678. (b) Lindsey, J. S.; Schreiman, I. C.; Hsu, H. C.; Kearney, P. C.; Marguerettaz, A. M. *J. Org. Chem.* **1987**, *52*, 827−836.

(8) Lin, C.-Y. Ph.D. Thesis, Princeton University, February, 1997.

(9) Brand, H.; Capriotti, J. A.; Arnold, J. *Inorg. Chem.* **1994**, *33*, 4334−4337.

(10) Burla, M. C.; Camalli, M.; Cascarano, G.; Giacovazzo, C.; Polidori, G.; Spagna, R.; Viterbo, D. *J. Appl. Crystallogr.* **1989**, *22*, 389−393.

Table 1. Summary of Structure Determination of [5,10,15,20-Tetrakis(heptafluoropropyl)porphinato]iron(II)·(Pyridine)$_2$

formula	$FeC_{42}H_{18}N_6F_{28}$
formula weight	1194.45
crystal class	monoclinic
space group	$P2_1/n$(No. 14)
Z	4
cell constants	
a	12.772(1) Å
b	18.895(2) Å
c	19.756(2) Å
β	99.960(6)°
V	4695.7(8) Å^3
μ	4.72 cm^{-1}
D_{calc}	1.689 g/cm^3
F(000)	2360.00
radiation	Mo Kα ($\lambda = 0.7107$ Å)
θ range	3.0−25.0°
h, k, l collected	±15, ±22, ±23
no. reflections measured	29068
no. unique reflections	7968 ($R_{merge} = 0.109$)
no. reflections used in refinement	5097 ($F^2 > 3.0\sigma$)
no. parameters	694
data/parameter ratio	7.34
R_1	0.096
R_2	0.097
GOF	2.85

unique reflections with $F^2 > 3\sigma(F^2)$ were used during subsequent structure refinement. Refinement was by full-matrix least squares techniques based on F to minimize the quantity $\sum w(|F_o| - |F_c|)^2$ with $w = 1/\sigma^2(F)$. Non-hydrogen atoms were refined anisotropically and hydrogen atoms were refined isotropically. Refinement converged to $R_1 = 0.096$ and $R_2 = 0.097$.

Results and Discussion

Structural Studies. The ORTEP representation of [5,10,15,20-tetrakis(heptafluoropropyl)porphinato]iron(II)·(pyridine)$_2$ [$(C_3F_7)_4PFe\cdot(py)_2$] is shown in Figure 1, with thermal ellipsoids displayed at 30% probability. The macrocycle possesses an S_4 ruffled structure, reminiscent of the X-ray crystallographic data previously reported for the $(C_3F_7)_4PH_2$ and the $(C_3F_7)_4PZn\cdot(py)$ complexes.[1a,b] The magnitude of the S_4 distortion for the $(C_3F_7)_4PFe\cdot(py)_2$ complex, however, is particularly severe. Comparison of the X-ray crystallographic data for these three compounds reveals that the average displacements of the C_{meso} carbon atoms from the least-squares plane defined by the four central nitrogen atoms vary from 0.618 to 0.405 to 0.294 Å, respectively, in the $(C_3F_7)_4PFe\cdot(py)_2$, $(C_3F_7)_4PZn\cdot(py)$, and $(C_3F_7)_4PH_2$ structures; similarly, the average displacements of the C_β carbon atoms from this plane range from 0.238 to 0.169 to 0.146 Å across this series of S_4-distorted porphyrin compounds. The magnitudes of the perpendicular displacements of all macrocyclic non-hydrogen atoms from the plane defined by the four porphyrinic nitrogens for $(C_3F_7)_4PFe\cdot(py)_2$ are represented diagrammatically in Figure 2. While steric congestion at the porphyrin periphery caused by the eight short H−F nonbonded contacts between the porphyrin β-hydrogens and the α-CF_2 fluorine atoms is a primary driving force for the strain-relieving S_4 structural perturbation,[1a,b] the larger S_4 distortion evinced for the $(C_3F_7)_4PFe\cdot(py)_2$ complex shown in Figure 2 undoubtedly derives from porphyrin ring contraction about the central iron atom.[11−13] The extent of ring contraction for $(C_3F_7)_4PFe\cdot(py)_2$ exceeds that observed for $(C_3F_7)_4PZn\cdot(py)$ for three

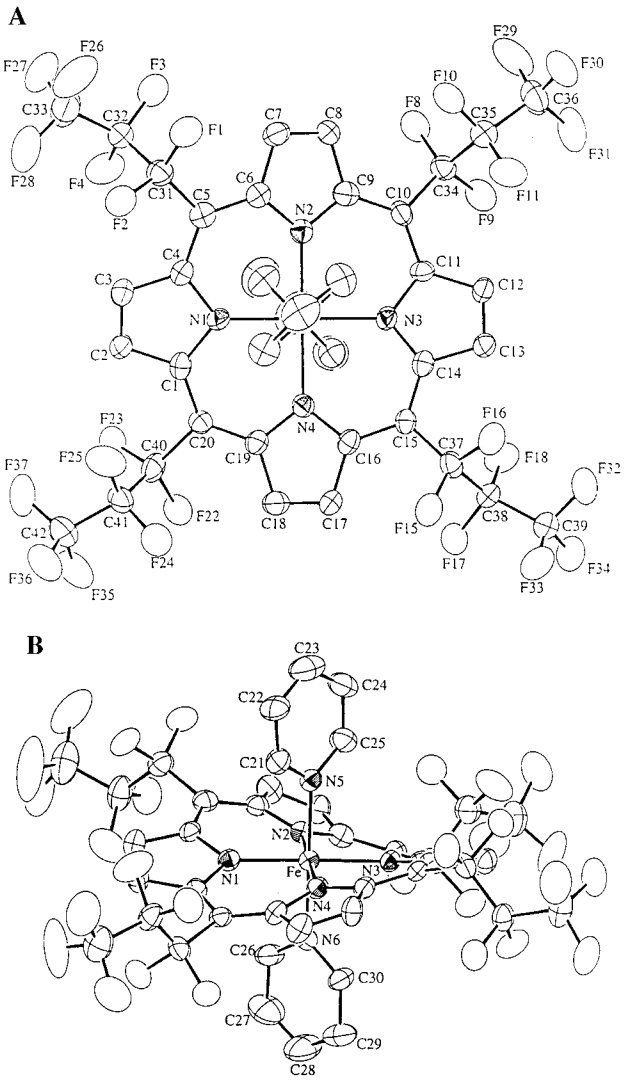

Figure 1. ORTEP views of [5,10,15,20-tetrakis(heptafluoropropyl)-porphinato]iron·(py)$_2$ with thermal ellipsoids at 30% probability, highlighting (A) the macrocycle plane, and (B) the relative positions of the axial pyridyl ligands.

reasons: (i) the atomic radius of Fe^{II} (1.26 Å) is diminished slightly with respect to Zn^{II} (1.38 Å); (ii) while the zinc atom domes the least-squares plane defined by the four pyrrolyl nitrogen atoms in the $(C_3F_7)_4PZn\cdot(py)$ structure, hexacoordination requires the analogous plane to contain the iron atom of $(C_3F_7)_4PFe\cdot(py)_2$ and maximize σ-symmetric orbital interactions with the electron-poor macrocycle; and importantly, (iii) enhanced ruffling in the $(C_3F_7)_4PFe\cdot(py)_2$ structure serves to augment the degree of in-plane electron density that can be accessed by the metal center with respect to a hypothetical structure having a non-S_4 distorted (flat) macrocycle (vide infra).

(11) (a) Scheidt, W. R.; Reed, C. A. *Chem Rev.* **1981**, *81*, 543−555. (b) Scheidt, W. R.; Gouterman, W. In *Iron Porphyrins*, Part II; Lever, A. B. P., Gray, H. B., Eds.; Addison-Wesley: MA, 1983; Chapter 1. (c) Scheidt, W. R.; Lee, Y. J. *Struct. Bonding* **1987**, *64*, 1−70. (d) Mansuy, D. *Coord. Chem. Rev.* **1993**, *125*, 129−142. (e) Momenteau, M.; Reed, C. A. *Chem. Rev.* **1994**, *94*, 659−698.

(12) (a) Li, N.; Coppens, P.; Landrum, J. *Inorg. Chem.* **1988**, *27*, 482−488. (b) Li, N.; Petricek, V.; Coppens, P.; Landrum, J. *Acta Crystallogr.* **1985**, *C41*, 902−905. (c) Safo, M. K.; Nesset, M. J. M.; Walker, F. A.; Debrunner, P. G.; Scheidt, W. R. *J. Am. Chem. Soc.* **1997**, *119*, 9438−9448.

(13) (a) Reed, C. A., Mashiko, T.; Bentley, S. P.; Kastner, M. E.; Scheidt, W. R.; Spartalian, K.; Lang, G. *J. Am. Chem. Soc.* **1979**, *101*, 2948−2958. (b) Inniss, D.; Soltis, S. M.; Strouse, C. E. *J. Am. Chem. Soc.* **1988**, *110*, 5644−5650. (c) Safo, M. K.; Gupta, G. P.; Walker, F. A.; Scheidt, W. R. *J. Am. Chem. Soc.* **1991**, *113*, 5497−5510. (d) Ivanca, M. A.; Lappin, A. G.; Scheidt, W. R. *Inorg. Chem.* **1991**, *30*, 711−718. (e) Safo, M. K.; Walker, F. A.; Raitsimring, A. M.; Walters, W. P.; Dolata, D. P.; Debrunner, P. G.; Scheidt, W. R. *J. Am. Chem. Soc.* **1994**, *116*, 7760−7770. (f) Munro, O. Q.; Marques, H. M.; Debrunner, P. G.; Mohanrao, K.; Scheidt, W. R. *J. Am. Chem. Soc.* **1995**, *117*, 935−954.

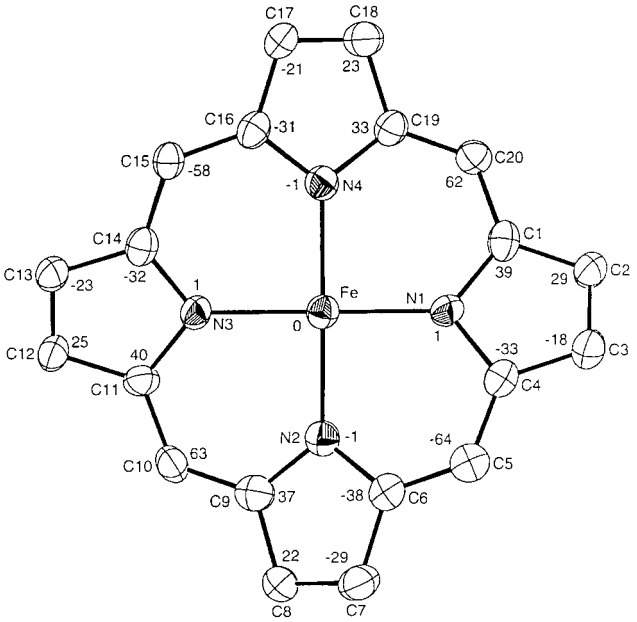

Figure 2. Diagrammatic representation of the porphyrin core of [5,10,15,20-tetrakis(heptafluoropropyl)porphinato]iron·(py)$_2$, illustrating the extent of the macrocycle S_4 distortion. The numbers adjacent to the atom labels signify the perpendicular displacements, in units of 0.01 Å, from the least-squares plane as defined by the four porphyrin nitrogen atoms.

Key structural similarities that are observed between $(C_3F_7)_4$PFe·(py)$_2$ and other reported low-spin PFe^{II}·(py)$_2$ structures include the in-plane orientation of the iron metal with respect to the four $N_{pyrrolyl}$ atoms, and the fact that the dihedral angle ϕ, which is defined as the angle made by a planar axial ligand with respect to the N−Fe−N vectors of the macrocycle,[11a,b] resembles that observed in analogous PFe^{II}·(L)$_2$ complexes.[12a,b] Major differences, however, are observed in all of the Fe−N bond lengths and the relative orientation of the pyridine ligands in $(C_3F_7)_4$PFe·(py)$_2$ with respect to all other previously obtained PFe^{II} structures. The unique metrical features of the structure have their origin in the special electronic properties of the $(C_3F_7)_4PH_2$ macrocycle[1] and cannot be attributed to any unusual packing forces in the $(C_3F_7)_4$PFe·(py)$_2$ crystal.[11]

Table 2 lists selected bond lengths and bond angles for the $(C_3F_7)_4$PFe·(py)$_2$ structure, while Table 3 compares key structural parameters for this compound with those for other crystallographically characterized, benchmark PFe complexes. As seen in Table 3, $(C_3F_7)_4$PFe·(py)$_2$ possesses Fe−$N_{pyrrolyl}$ and Fe−$N_{pyridyl}$ bond distances approximately 0.04 ± 0.006 Å shorter than the analogous distances observed for the structurally characterized 5,10,15,20-tetraphenyl(porphinato)iron(II)·(pyridine)$_2$ [$(C_6H_5)_4$PFe·(py)$_2$] complex.[12a,b] Also remarkable in Table 3 is the fact that the pyridine ligands are eclipsed in $(C_6H_5)_4$PFe·(py)$_2$, which features a relatively planar porphyrin macrocycle, while they are staggered (orthogonal) in the severely S_4-ruffled $(C_3F_7)_4$PFe·(py)$_2$ structure. It is important to note that the metrical parameters observed for $(C_6H_5)_4$PFe·(py)$_2$ typify that evinced for other crystallographically characterized PFe^{II}·L$_2$ species,[12c] thereby underscoring these novel aspects of the $(C_3F_7)_4$PFe·(py)$_2$ structure.

Comparison of the X-ray crystallographic data obtained for the *ferrous* $(C_3F_7)_4$PFe·(py)$_2$ compound with those of a variety of structurally characterized, low spin *ferric* $(C_6H_5)_4$PFe^{III}·(pyridine)$_2$ complexes reveal striking similarities in terms of Fe−$N_{pyrrolyl}$ bond lengths, metal-to-axial ligand distances, the magnitude of the macrocyclic S_4 distortion, and axial ligand torsional angles.[13] Metrical data reported for $[(C_6H_5)_4$PFe·(py)$_2]^+$ $[(ClO_4)]^-$ and those for an analogous complex that features 4-cyanopyridyl (4-CN-py) axial ligands are highlighted in Table 3. Intriguingly, the Fe−$N_{pyridyl}$ and Fe−$N_{pyrrolyl}$ bond distances are virtually identical in the $[(C_6H_5)_4$PFe·(4-CN-py)$_2]^+$ $[(ClO_4)]^-$[13e] and $(C_3F_7)_4$PFe·(py)$_2$ structures, although the degree of macrocycle S_4 ruffling is more pronounced for $(C_3F_7)_4$PFe·(py)$_2$; moreover, both complexes exhibit axial pyridyl ligands that are mutually staggered with respect to each other.

Table 2. Selected Bond Distances and Bond Angles for [5,10,15,20-Tetrakis(heptafluoropropyl)porphinato]iron(II)·(Pyridine)$_2$

bond	distance, Å	bond	distance, Å
Fe−N_1	1.940(6)	N_4−C_{16}	1.357(9)
Fe−N_2	1.951(6)	N_4−C_{19}	1.390(9)
Fe−N_3	1.959(6)	C_1−C_2	1.434(10)
Fe−N_4	1.981(6)	C_1−C_{20}	1.381(10)
Fe−N_5	2.007(6)	C_{10}−C_{11}	1.388(10)
Fe−N_6	1.996(6)	C_{11}−C_{12}	1.441(10)
F_1−C_{31}	1.358(9)	C_{12}−C_{13}	1.319(11)
F_2−C_{31}	1.362(9)	C_{13}−C_{14}	1.458(10)
N_1−C_1	1.417(9)	C_{14}−C_{15}	1.408(10)
N_1−C_4	1.387(9)	C_{20}−C_{40}	1.538(11)
angle	**angle, deg**	**angle**	**angle, deg**
N_1−Fe−N_2	90.2(2)	N_1−C_1−C_2	108.2(7)
N_1−Fe−N_3	179.6(2)	N_1−C_1−C_{20}	122.4(7)
N_1−Fe−N_5	89.1(2)	C_2−C_1−C_{20}	128.6(7)
N_1−Fe−N_6	90.4(3)	C_1−C_2−C_3	108.4(7)
N_2−Fe−N_5	89.3(2)	C_1−C_{20}−C_{19}	125.5(7)
N_2−Fe−N_6	90.2(3)	C_1−C_{20}−C_{40}	115.5(7)
Fe−N_1−C_1	127.4(5)	F_{22}−C_{40}−F_{23}	102.4(7)
Fe−N_1−C_4	127.2(5)	C_{20}−C_{40}−C_{41}	118.5(7)
C_1−N_1−C_4	105.4(6)	F_{24}−C_{41}−F_{25}	105.2(8)

While all low-spin, structurally characterized PFe^{III} species are ruffled with staggered axial ligands, Scheidt, Walker, and Debrunner have noted that the degree of porphyrin macrocycle ruffling increases with decreased σ-donating and increased π-accepting abilities of axial pyridyl groups.[12c,13e] For highly ruffled PFe^{III} structures, a $(d_{xz},d_{yz})^4(d_{xy})^1$ electronic configuration becomes stabilized with respect to the more commonly observed $(d_{xy})^2(d_{xz},d_{yz})^3$ ground state. In such structures, any increased delocalization of the metal-centered electron density via interaction of the d_{xz} and d_{yz} orbitals with the staggered axial ligand π^* sets is attenuated by the diminished interaction of the metal d_{xz},d_{yz} with the macrocycle frontier orbitals and the enhanced overlap of the metal d_{xy} with the porphyrin a_{2u}; the importance of these perturbations to metal−ligand bonding interactions increases concomitantly with augmented ruffling. Congruently, Table 3 shows that the bis(4-CN-py) derivative of $(C_6H_5)_4$PFe^{III} is considerably more ruffled than its bis(pyridine) analogue.

Clearly, for $(C_3H_7)_4$PFe·(py)$_2$, electronic interactions other than those involving axial ligands must be responsible for the genesis of this structure. Several lines of reasoning support this supposition. First, the π-accepting ability of pyridine is exceedingly modest relative to 4-CN-py; hence π-back-bonding interactions involving the d_{xz} and d_{yz} orbitals can neither play a role in stabilizing the ruffled structure nor account for the short metal−pyridyl bond in $(C_3F_7)_4$PFe·(py)$_2$. Second, the argument that crystal field effects deriving from axial ligand basicity are the origin of the stabilization of d_{xz} and d_{yz} relative to d_{xy} in highly ruffled PFe^{III} structures cannot be made for the $(C_3F_7)_4$PFe·(py)$_2$ complex because the acidity constant for pyridine exceeds that of 4-CN-py by nearly 4 orders of magnitude.[14] Third, the fact that the Fe−$N_{pyridyl}$ bond distances are equal in

(14) Fisher, A.; Galloway, W. J.; Vaughan, J. *J. Chem. Soc.* **1964**, 3591−3596.

Table 3. Metrical Parameters for Porphinato(Iron)·$(py)_2$ Systems

compd	Fe−$N_{pyrrole}$ distance (Å)	Fe−$N_{pyridine}$ distance (Å)	dihedral angle, ϕ, deg[e]	axial ligand torsional angle[f]	bis$(L)_2$ relative orientation, deg[g]	average C_{meso} displacement (Å)[h]	reference
$(C_3F_7)_4$PFe·$(py)_2$	1.958	2.002	41.3 46.0	84.72 89.12	87.5	0.62	this work
$(C_6H_5)_4$PFe·$(py)_2$[a]	2.001	2.037	43.12 34.4	74.74	4.8	0.15	12a
$(C_6H_5)_4$PFe·$(py)_2$ 2Py[b]	1.993	2.039	34.4	87.46	0.0	0.06	12b
$[(C_6H_5)_4$PFe·$(py)_2]^+$ $[ClO_4]^-$[c]	1.982	2.003	34 52	80.66 80.64	84.9	0.25	13b
$[(C_6H_5)_4$PFe·(4-CN-$py)_2]^+$ $[ClO_4]^-$[d]	1.952	2.002	35 36	86.9 86.6	∼90	0.55	13e

[a] $(C_6H_5)_4$PFe·$(py)_2$ = [5,10,15,20-tetraphenylporphinato]iron(II)·$(py)_2$. [b] $(C_6H_5)_4$PFe·$(py)_2$ 2Py = [5,10,15,20-tetraphenylporphinato]iron(II)·$(py)_2$ bis(pyridine) solvate. [c] $[(C_6H_5)_4$PFe·$(py)_2]^+$ $[ClO_4]^-$ = [(5,10,15,20-tetraphenylporphinato)iron·$(py)_2]^+[ClO_4]^-$. [d] $[(C_6H_5)_4$PFe·(4-CN-$py)_2]^+$ $[ClO_4]^-$ = [(5,10,15,20-tetraphenylporphinato)iron·(4-cyanopyridine)$_2]^+[ClO_4]^-$. [e] Defined as the angle made by the axial ligand plane with respect to the N−Fe−N vectors of the macrocycle. [f] Defined as the torsional angle between the axial ligand with the macrocycle least-squares plane. [g] Defined as the torsional angle between two planar axial ligands. [h] Defined as the average value of *meso*-carbon atom displacement from the porphyrin mean plane.

the $[(C_6H_5)_4$PFe·(4-CN-$py)_2]^+$ $[(ClO_4)]^-$ and $(C_3F_7)_4$PFe·$(py)_2$ structures while the ferrous structure is significantly more ruffled, argues against any simple correlation with the degree of porphyrin ruffling and the length of the metal−pyridyl bond. Finally, all other crystallographically characterized [5,10,15,-20-tetra(substituted)porphinato]iron(II)·$(L)_2$ species examined to date evince either planar porphyrin ligands or macrocycles with modest degrees of ruffling.[12] Macrocycle electronic properties must thus play a primary role in determining the large degree of ruffling observed in the $(C_3F_7)_4$PFe·$(py)_2$ structure.

While one would have predicted that a $(C_3F_7)_4$PFe·$(py)_2$ X-ray crystallographic structure would have been ruffled based simply upon the steric requirements of the *meso*-perfluoroalkyl group,[1a,b] the severity of the ruffling distortion argues that electronic factors play a role in the stabilization of this unusual ferrous porphyrin structure. Given that $[(C_6H_5)_4$PFe·(4-CN-$py)_2]^+$ $[(ClO_4)]^-$ possesses a $(d_{xz},d_{yz})^4(d_{xy})^1$ ground-state electronic configuration and that all of the metrical parameters that characterize the ferrous $(C_3F_7)_4$PFe·$(py)_2$ and ferric $[(C_6H_5)_4$-PFe·(4-CN-$py)_2]^+$ $[(ClO_4)]^-$ structures are strikingly similar, it is probable that electronic modulation of the metal center by the macrocycle enforces a ground-state electronic configuration of $(d_{xz},d_{yz})^4(d_{xy})^2$ for $(C_3F_7)_4$PFe·$(py)_2$ (vide infra). Previous electrochemical and XPS studies substantiate extreme stabilization of the macrocycle π and σ systems by the *meso*-perfluoroalkyl groups;[1b] the structural data thus appear congruent with the electronic properties of these *meso*-appended moieties which facilitate removal of macrocycle-localized electron density via the σ bonding network.

What factors drive the extensive ferrous porphyrin ruffling and the stabilization of a $(d_{xz},d_{yz})^4(d_{xy})^2$ ground state? Certainly, a S_4 distortion reduces the overlap of the iron (d_{xz},d_{yz}) set with the macrocycle's e_g symmetric LUMO; furthermore, such distortions abate the degree of porphyrin ring aromaticity. Despite the fact that the diminution of the important metal (d_{xz},d_{yz}) → porphyrin (e_g) MLCT interaction is partly compensated by the increased interaction of the metal d_{xy} with the porphyrin e_g symmetric LUMO in $(C_3F_7)_4$PFe·$(py)_2$, ruffling distortions must nonetheless be net destabilizing with respect to the π system of this complex. The electronic driving force for augmented ruffling observed in $(C_3F_7)_4$PFe·$(py)_2$ relative to the $(C_3F_7)_4$PZn·(py) and $(C_3F_7)_4PH_2$ structures and other [5,10,15,20-tetra(substituted)porphinato]iron(II)·$(L)_2$ systems must derive from an increased stabilization of lower-lying filled σ-symmetric bonding and nonbonding orbitals with respect to those complexes that manifest more-planar porphyrin macrocyclic structures; this is reasonable given that large ruffling distortions permit the normally orthogonal porphyrin π-symmetric orbitals to participate in in-plane bonding interactions with the metal. Congruent with this argument, because *meso*-perfluoroalkyl substituents make the pyrrolyl nitrogen-centered electrostatic potentials significantly more positive (as evinced from XPS data[1b]), such an increase in metal in-plane electron density driven by the ruffled porphyrin structure would assuredly serve to enhance the electrostatic stability of the $(C_3F_7)_4$PFe·$(py)_2$ complex.

Likewise, the short Fe−$N_{pyrrolyl}$ and Fe−$N_{pyridyl}$ bond lengths observed in the $(C_3F_7)_4$PFe·$(py)_2$ structure thus derive from the non-π-conjugating, exceptional σ-electron withdrawing properties of the *meso*-fluorocarbon substituents. While mutually staggered pyridines enable optimal overlap of the d_{xz} and d_{yz} orbitals of the iron atom with the π*-symmetric orbitals of the axial ligands, the factors responsible for the short (2.002 Å) Fe−$N_{pyridyl}$ bonds are the depleted electron density in the macrocycle σ system and the significant Lewis basicity of the pyridine (pK_a = 5.21); hence, the short metal−pyridyl bond in this ferrous porphyrin derives from augmented σ overlap of the axial pyridines with the electron deficient metal center. In line with this discussion, the origin of the mutually orthogonal relationship of the axial pyridyl groups deserve further comment. As recently elucidated by Scheidt and Walker,[12c] X-ray crystallographic studies of [5,10,15,20-tetra(mesityl)porphinato]Fe·(4-CN-$py)_2$ show that this species contrasts its ferric porphyrin analogue in that it exhibits a relatively planar macrocycle with eclipsed axial ligands, underscoring the unimportance of metal−axial ligand π-back-bonding in this ferrous porphyrin structure. Congruent with earlier molecular mechanics calculations for ruffled PFe complexes,[13e,g] analogous MM2 calculations parametrized for hexacoordinate transition-metal complexes indicate that the lowest energy conformation for the severely S_4-ruffled $(C_3F_7)_4$PFe·$(py)_2$ structure coincides with an orthogonal orientation for the axial pyridines (data not shown); this point has been made previously by Strouse,[13b] who noted that the staggered orientation of the pyridyl ligands in the modestly ruffled $[(C_6H_5)_4$PFe·$(py)_2]^+$ $[(ClO_4)]^-$ structure is the sterically most favorable configuration (Table 3). Because the porphyrin ring is always destabilized by ruffling in ferric and ferrous porphyrin structures,[12c] it is a reasonable supposition that in the absence of steric effects (e.g., bulky axial ligands, highly substituted porphyrin peripheries), electronic modulation of the metal center via the porphyrin substituents or axial ligands will determine both the ground-state metal electronic configuration and the degree to which the macrocycle ruffles to enhance in-plane bonding interactions. Once electronic parameters dictate

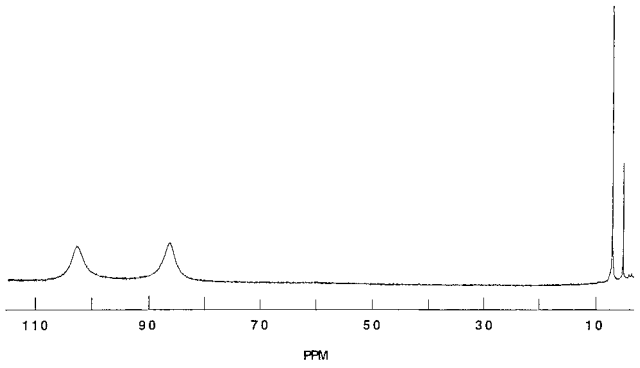

Figure 3. ^{1}H NMR spectrum of [5,10,15,20-tetrakis(heptafluoropropyl)-porphinato]iron·chloride in $CDCl_3$. Chemical shifts are relative to solvent residual protium ($\delta = 7.24$ ppm).

a significant degree of ruffling, a staggered orientation of planar axial ligands (pyridines, imidazoles) will generally be manifest in the solid state as this orientation minimizes nonbonded interactions between the axial groups and the porphyrin macrocycle.

The similarities between $(C_3F_7)_4PFe\cdot(py)_2$ and structurally characterized $PFe^{III}\cdot(L)_2$ complexes suggest that while the metal oxidation state of $(C_3F_7)_4PFe\cdot(py)_2$ is formally Fe^{II}, the *meso*-heptafluoropropyl porphyrin substituents enable such effective removal of metal-centered electron density that this PFe^{II} complex uniquely exhibits the hallmarks of a ferric porphyrin species in the solid state. Given the points discussed above, it will be interesting to probe how better π-back-bonding axial ligands, superior axial σ-donors, more highly R_f-substituted macrocycles, and metal oxidation state impact the degree to which the porphyrin core is ruffled for this class of electron-deficient (porphinato)metal species.

^{1}H NMR Studies. In solution, ^{1}H NMR analysis of $(C_3F_7)_4PFe\cdot(py)_2$ indicates that the six-coordinate complex is low spin, consistent with the strong ligand field stabilization of the iron d_{xz} and d_{yz} orbitals generally observed for PFe^{II} complexes featuring two nitrogenous Lewis bases as axial ligands.[11−13] The β protons of $(C_3F_7)_4PFe\cdot(py)_2$ are shifted 0.5 ppm upfield from the corresponding ^{1}H NMR signals for the β nuclei in $(C_3F_7)_4PZn$ and $(C_3F_7)_4PH_2$,[1] an observation congruent with the decreased macrocycle aromaticity that results from the significantly more pronounced S_4 ruffling in the PFe species. The ligated pyridine ortho, meta, and para signals ($\delta = 2.09$, 4.97, and 5.95 ppm, respectively) are shifted upfield from the analogous proton resonances for free pyridine in $CDCl_3$ (δ ortho, meta, and para = 8.60, 7.20, and 6.80 ppm). The magnitude and direction of the pyridine shifts in $(C_3F_7)_4PFe\cdot(py)_2$ relative to uncomplexed pyridine are similar to those observed for the $(C_6F_5)_4PFe\cdot(py)_2$ complex,[1c,d] as well as the previously characterized six-coordinate 5,10,15,20-tetraphenyl(porphinato)-ruthenium(II)·(pyridine)$_2$ system described by Collman.[15] Thus, these chemical shift values appear not to be significantly affected by steric properties of the porphyrin macrocycle, as $(C_6H_5)_4PRu\cdot(py)_2$ possesses a planar structure in contrast to that observed for $(C_3F_7)_4PFe\cdot(py)_2$.

Figure 3 displays the ^{1}H NMR spectrum for the [5,10,15,-20-tetrakis(heptafluoropropyl)porphinato]iron(III)·chloride [$(C_3F_7)_4PFe\cdot Cl$] complex; the β-protons show isotropic shifts on the order of 80−100 ppm. Spectroscopically characterized $S = {}^5/_2$ (porphinato)iron(III)·chloride systems typically possess β-proton ^{1}H NMR resonances between 70 and 90 ppm; it has been shown that the large downfield shifts of these signals from that observed for their diamagnetic, $S = 0$ Fe(II) analogues derive from both through-bond contact and through-space dipolar interactions.[16,17] A S_4-distortion lowers the symmetry of $(C_3F_7)_4PFe\cdot Cl$ to C_{2v}; interestingly, two sets of β-proton resonances ($\delta = 101.5$ and 86.4 ppm) are observed, confirming that the macrocycle maintains a highly nonplanar structure in solution and contrasting data reported for C_{4v}-symmetric $(C_6F_5)_4PFe\cdot Cl$, which displays only a single β-proton NMR signal ($\delta = 82$ ppm).[1d,17g] The 15 ppm chemical shift difference between the β-H resonances of $(C_3F_7)_4PFe\cdot Cl$ must be contact in origin, as ruffling only creates a ∼0.1 Å difference in the relative distances between these nuclei and the iron center.

^{19}F NMR Studies. ^{19}F NMR spectroscopy has been previously shown to provide considerable insight into the electronic structure of metalated and free ligand forms of *meso*-perfluorophenylporphyrins; these systems are characterized by multiple, chemically distinct fluorine resonances that are readily observed due to the near 100% natural abundance and high gyromagnetic ratio of ^{19}F.[18] We have employed ^{19}F NMR spectroscopy to probe the electronic structure of *meso*-perfluoroalkyl substituted porphyrins and their (porphinato)iron complexes; Figure 4A shows the assignments of ^{19}F resonances for $(C_3F_7)_4PH_2$. The γ-CF_3 signal is observed at −79 ppm, a value typical for a CF_3 resonance in a perfluoroalkyl chain composed of three or more carbon atoms; likewise, the β-CF_2 resonances are observed at −119 ppm, in accord with that found for the β-CF_2 signals of perfluoroalkyl-substituted arenes.[18a] The α-CF_2 resonance for $(C_3F_7)_4PH_2$ appears at −80 ppm and is clearly the most affected by steric and electronic properties of the porphyrin macrocycle; it is noteworthy that the $(C_3F_7)_4PH_2$ α-CF_2 resonance is shifted approximately 30 ppm downfield from the analogous ^{19}F NMR signal in heptafluoropropylbenzene.

While the chemical shift values for the β-CF_2 and γ-CF_3 fluorine atoms are similar, the α-CF_2 resonance in the ^{19}F NMR spectrum of Aoyagi's 2,7,12,17-tetrakis(heptafluoropropyl)-porphyrin occurs at $\delta = -99.1$ ppm, nearly 20 ppm upfield of the same resonance in $(C_3F_7)_4PH_2$.[18b] Clearly, the magnitude of the ^{19}F NMR resonance frequency for the α-CF_2 fluorine atoms that are directly fused to an aromatic framework is a sensitive reporter of electronic structure. Factors that likely account for the variance in α-CF_2 chemical shifts in these species include the fact that the tetrakis(β-perfluoroalkyl)porphyrin ligand is planar, and only moderately more electron deficient than the parent porphyrin macrocycle;[18d] hence, the α-CF_2 resonance frequency more closely resembles that observed for C_3F_7-substituted benzene. Furthermore, the large downfield shift

(15) (a) Collman, J. P.; Barnes, C. E.; Swepston, P. N.; Ibers, J. A. *J. Am. Chem. Soc.* **1984**, *106*, 3500−3510. (b) Collman, J. P.; Barnes, C. E.; Collins, T. J.; Brothers, P. J.; Gallucci, J.; Ibers, J. A. *J. Am. Chem. Soc.* **1981**, *103*, 7030−7032.

(16) Goff, H. In *Iron Porphyrins*, Part I.; Lever, A. B. P., Gray, H. B., Eds.; Addison-Wesley: MA, 1983; Chapter 4.

(17) (a) Mispelter, J.; Momenteau, M.; Lhoste, J. M. *J. Chem. Phys.* **1980**, *72*, 1003−1012. (b) Mispelter, J.; Momenteau, M.; Lhoste, J. M. *Mol. Phys.* **1977**, *33*, 1715−1728. (c) Behere, D. V.; Birdy, R.; Mitra, S. *Inorg. Chem.* **1982**, *21*, 386−390. (d) Safo, M. K.; Gupta, G. P.; Watson, C. T.; Simonis, U.; Walker, F. A.; Scheidt, W. R. *J. Am. Chem. Soc.* **1992**, *114*, 7066−7075. (e) Tan, H.; Simonis, U.; Shokhirev, N. V.; Walker, F. A. *J. Am. Chem. Soc.* **1994**, *116*, 5784−5790. (f) Wolowiec, S.; Latos-Grazynski, L. *Inorg. Chem.* **1994**, *33*, 3576−3586. (g) Cheng, R.-J.; Latos-Grazynski, L.; Balch, A. L. *Inorg. Chem.* **1982**, *21*, 2412−2418.

(18) (a) Webb, G. A. *Annual Reports on NMR Spectroscopy*; Academic Press: New York, 1983; Vol. 14. (b) Aoyagi, K.; Toi, H.; Aoyama, Y.; Ogoshi, H. *Chem. Lett.* **1988**, 1891−1894. (c) Birnbaum, E. R.; Hodge, J. A.; Grinstaff, M. W.; Schaefer, W. P.; Henling, L.; Labinger, J. A.; Bercaw, J. E.; Gray, H. B. *Inorg. Chem.* **1995**, *34*, 3625−3632. (d) Ono, N.; Kawamura, H.; Maruyama, K. *Bull. Chem. Soc. Jpn.* **1989**, *62*, 3386−3388. (e) Yoshimura, T.; Toi, H.; Inaba, S.; Ogoshi, H. *Inorg. Chem.* **1991**, *30*, 4315−4321.

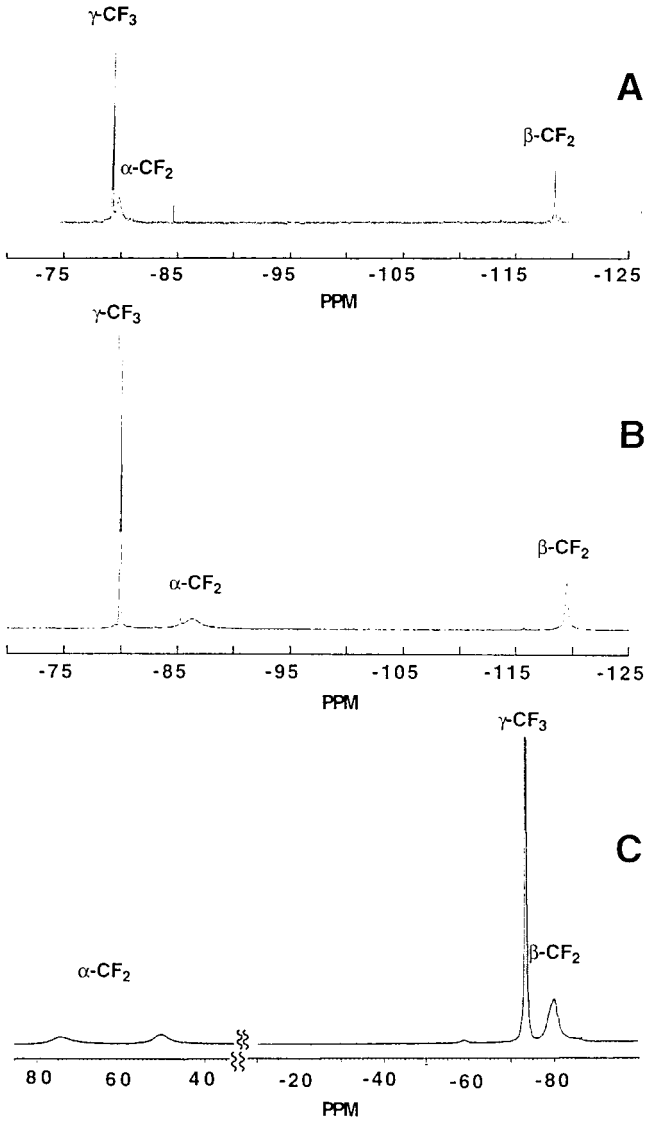

Figure 4. ^{19}F NMR spectra of (A) 5,10,15,20-tetrakis(heptafluoropropyl)porphyrin, (B) [5,10,15,20-tetrakis(heptafluoropropyl)porphinato]iron·$(py)_2$, and (C) [5,10,15,20-tetrakis(heptafluoropropyl)porphinato]iron·chloride. Chemical shifts are relative to $CFCl_3$ ($\delta = 0$ ppm) in $CDCl_3$.

of the α-CF_2 fluorines of $(C_3F_7)_4PH_2$ relative to those of tetrakis(β-perfluoroheptyl)porphyrin is a direct consequence of the disparate electronic properties of these two macrocycles: $(C_3F_7)_4PH_2$ is appreciably more electron-deficient than tetrakis(β-perfluoroheptyl)porphyrin,[1a,b] although the magnitude of this difference is probably attenuated to some degree by the decreased aromaticity of the highly ruffled $(C_3F_7)_4PH_2$ ligand.

Electronic differences between the $(C_3F_7)_4PFe\cdot(py)_2$ and $(C_3F_7)_4PH_2$ compounds are manifest in the ^{19}F NMR spectra (Figure 4A−B). While the γ-CF_3 and β-CF_2 fluorine signals for $(C_3F_7)_4PFe\cdot(py)_2$ exhibit shifts on the order of 1 ppm relative to those observed for $(C_3F_7)_4PH_2$, the α-CF_2 resonance is shifted upfield by 6.2 ppm ($\delta = -86.2$ ppm), consistent with the fact that the macrocycle of the $(C_3F_7)_4PFe\cdot(py)_2$ complex is more ruffled in solution. The broad line width of this resonance derives from conformational dynamics that elevatate the barrier to rotation about the CF_2-C_{meso} bond in the highly S_4-distorted $(C_3F_7)_4PFe\cdot(py)_2$ complex relative to the free porphyrin ligand; variable temperature NMR studies for $(C_3F_7)_4PFe\cdot(py)_2$ reveal that this resonance sharpens with increasing temperature.[1c,d]

Due to the high spin paramagnetic iron center, the ^{19}F NMR spectra of $(C_3F_7)_4PFe\cdot Cl$ manifests both broad resonances and impressive downfield shifts of the α-CF_2, β-CF_2, and γ-CF_3 ^{19}F resonances (Figure 4C) with respect to that observed for both $(C_3F_7)_4PFe\cdot(py)_2$ and the metal-free ligand. Note that the α-CF_2 fluorine atoms resonate at 75.46 and 51.76 ppm, more than 135 ppm downfield from the α-CF_2 signal of $(C_3F_7)_4PFe\cdot(py)_2$ (Figure 4B); the fact that the fluorine atoms are chemically inequivalent indicates that rotation about the CF_2-C_{meso} bond is slow with respect to the NMR time scale and that steric barriers for this process in $(C_3F_7)_4PFe\cdot Cl$ likely exceed that for $(C_3F_7)_4PFe\cdot(py)_2$. ^{19}F NMR signals are observed for the β-CF_2 and γ-CF_3 fluorine atoms of $(C_3F_7)_4PFe\cdot Cl$ at −73.75 and −80.17 ppm, respectively; these signals are shifted downfield 39.20 and 6.22 ppm with respect to their corresponding resonances in $(C_3F_7)_4PFe\cdot(py)_2$.

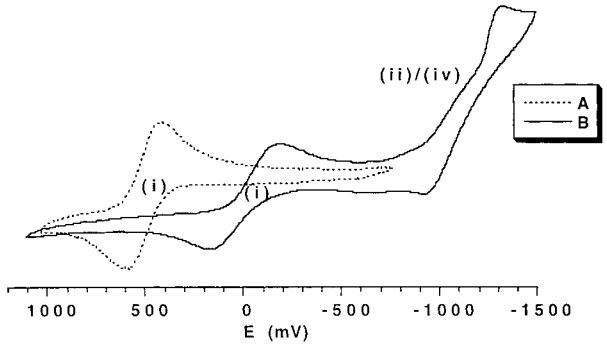

Figure 5. Cyclic voltammetric responses of (A) [5,10,15,20-tetrakis(heptafluoropropyl)porphinato]iron·$(py)_2$ and (B) [5,10,15,20-tetrakis(heptafluoropropyl)porphinato]iron·chloride recorded in benzonitrile highlighting the chemically reversible $Fe^{II/III}$ redox couples. Experimental conditions are described in Table 4.

Cyclic Voltammetric Studies Probing the $Fe^{II/III}$ Redox Couple. Cyclic voltammetric responses of 5,10,15,20-tetrakis(heptafluoropropyl)porphinato]iron complexes $(C_3F_7)_4PFe\cdot(py)_2$ and $(C_3F_7)_4PFe\cdot Cl$ (Figure 5A and B) exhibit current vs potential profiles consistent with those observed for previously studied $PFe^{II}\cdot(L)_2$ and $PFe\cdot Cl$ compounds at solid working electrodes.[19−21] The $Fe^{II/III}$ redox couple for $(C_3F_7)_4PFe\cdot Cl$ displayed in Figure 5B is observed at a potential of −10 mV in benzonitrile relative to SCE [supporting electrolyte = 0.1 M tetra-*n*-butylammonium perchlorate (TBAP)]; this potential is 90 mV more positive than that observed for $(C_6F_5)_4PFe\cdot Cl$ [$E_{1/2}$ ($Fe^{II/III}$) = −100 mV vs SCE] measured in the same solvent, and 400 mV more positive than observed for $(C_6H_5)_4PFe\cdot Cl$ [$E_{1/2}$ ($Fe^{II/III}$) = −410 mV vs

(19) (a) Wijesekera, T.; Matsumoto, A.; Dolphin, D.; Lexa, D. *Angew. Chem. Int. Ed. Engl.* **1990**, *29*, 1028−1030. (b) Binstead, R. A.; Crossley, M. J.; Hush, N. S. *Inorg. Chem.* **1991**, *30*, 1259−1264. (c) D'Souza, F.; Villard, A.; Van Caemelbecke, E.; Franzen, M.; Boschi, T.; Tagliatesta, P.; Kadish, K. M. *Inorg. Chem.* **1993**, *32*, 4042−4048. (d) Reddy, D.; Ravikanth, M.; Chandrashekar, T. K. *J. Chem. Soc., Dalton Trans.* **1993**, 3575−3580. (e) Kadish, K. M.; D'Souza, F.; Villard, A.; Autret, M.; Van Caemelbecke, E.; Bianco, P.; Antonini, A.; Tagliatesta, P. *Inorg. Chem.* **1994**, *33*, 5169−5170. (f) Hodge, J. A.; Hill, M. G.; Gray, H. B. *Inorg. Chem.* **1995**, *34*, 809−812. (g) Zanello, P.; Cinquantini, A.; Mangani, S.; Opromolla, G.; Pardi, L.; Janiak, C.; Rausch, M. D. *J. Organomet. Chem.* **1994**, *471*, 171−177. (h) Ochsenbein, P.; Ayougou, K.; Mandon, D.; Fischer, J.; Weiss, R.; Austin, R. N.; Jayaraj, K.; Gold, A.; Terner, J.; Fajer, J. *Angew. Chem., Int. Ed. Engl.* **1994**, *33*, 348−350. (i) Chen, H. L.; Ellis, P. E., Jr.; Wijesekera, T.; Hagan, T. E.; Groh, S. E.; Lyons, J. E.; Ridge, D. P. *J. Am. Chem. Soc.* **1994**, *116*, 1086−1089.

(20) Kadish, K. M. In *Iron Porphyrins*, Part II; Lever, A. B. P., Gray, H. B., Eds.; Addison-Wesley: MA, 1983; Chapter 4.

(21) (a) Choi, I.-K.; Ryan, M. D. *Inorg. Chim. Acta* **1988**, *153*, 25−30. (b) Geiger, D. K. *J. Chem. Educ.* **1991**, *68*, 340−342. (c) Srivatsa, S. G.; Sawyer, D. T. *Inorg. Chem.* **1985**, *24*, 1732−1734. (d) Constant, L. A.; Davis, D. G. *Anal. Chem.* **1975**, *47*, 2253−2260. (e) Nesset, M. J. M.; Shokhirev, N. V.; Enemark, P. D.; Jacobson, S. E.; Walker, F. A. *Inorg. Chem.* **1996**, *35*, 5188−5200. (f) Gueutin, C.; Lexa, D.; Momenteau, M.; Savéant, J.-M.; Xu, F. *Inorg. Chem.* **1986**, *25*, 4294−4307.

Table 4. Comparative Cyclic Voltammetric Data for Porphinato(iron)Systems Based on $(C_3F_7)_4PH_2$, $Br_8(C_6F_5)_4PH_2$, $(C_6F_5)_4PH_2$, and $(C_6H_5)_4PH_2$ Macrocycles[a]

			potentials (mV)			binding constants[d]	
PFe species	axial ligand	[py] (M)	$[PFe]^{0/+}$ [b]	$[PFe]^{0/-}$ [b]	$[PFe]^{-/2-}$ [c]	log $K_{Fe(II)}$	log($K_{Fe(III)}/K_{Fe(II)}$)
$(C_3F_7)_4PFe$	Cl	0	−10	−1120	−1120		
	$(py)_2$	0.001	+510	−1002	−1120	>4.7[g]	−9.2
	$(py)_2$	1.0	+540	−1060	*f*		
	$(py)_2$	neat	+580	−1060	*f*		
$Br_8(C_6F_5)_4PFe$[e]	Cl	0	+290	−650	−1140	2.7	−8.2
	$(py)_2$	1.0	+780	−810	−1050		
$(C_6F_5)_4PFe$[e]	Cl	0	−100	−980	−1280[e]	5.7[h]	−8.0
	$(py)_2$	0.001	+250	−1290	−1680		
	$(py)_2$	1.0	+370	−1220	−1660		
$(C_6H_5)_4PFe$[e]	Cl	0	−410	−1200	*f*	5.2	−7.9
	$(py)_2$	1.0	+50	−1510	*f*		

[a] Experimental conditions: [PFe] = 5 mM; [TBAP] = 0.1 M; solvent = benzonitrile; scan rate = 500 mV/s; reference electrode = Ag wire. Potentials reported are relative to SCE; the ferrocene/ferrocenium redox couple (+0.43 V vs SCE) was used as the internal standard. [b] Potentials reported are $E_{1/2}$ values. [c] Potentials reported are E_{pc} values. [d] Binding constants (log $K_{Fe(II)}$ and log $K_{Fe(III)}$) were calculated from the magnitude of the $PFe^{II/I}$ and $PFe^{III/II}$ $E_{1/2}$ values using eqs 5 and 6; experimental uncertainties in these values are typically ±0.2. Values reported for $(C_6H_5)_4PFe$ are similar to those reported earlier by Kadish. See ref 22. [e] Electrochemical data for $(C_6F_5)_4PFe{\cdot}Cl$, $Br_8(C_6F_5)_4PFe{\cdot}Cl$, and $(C_6H_5)_4PFe{\cdot}Cl$ have been reported for a variety of experimental conditions and are consistent with data reported here; see for example refs 4l, 18c, 19f, and 20. [f] Redox process occurs outside the solvent/electrolyte potential window. [g] The axial pyridyl binding constant evaluated from variable temperature NMR spectroscopic data is $3.0 \pm 0.6 \times 10^9$ (log $K_{Fe(II)} = 9.5 \pm 1.9$). See ref 1d. [h] Due to the large peak separation between the E_{pc} and E_{pa} values that define the $Fe^{II/I}$ redox couple, binding constants for this system were estimated from the axial ligand concentration-dependent $Fe^{II/I}$ cathodic peak shift as described by Kadish (see ref 20).

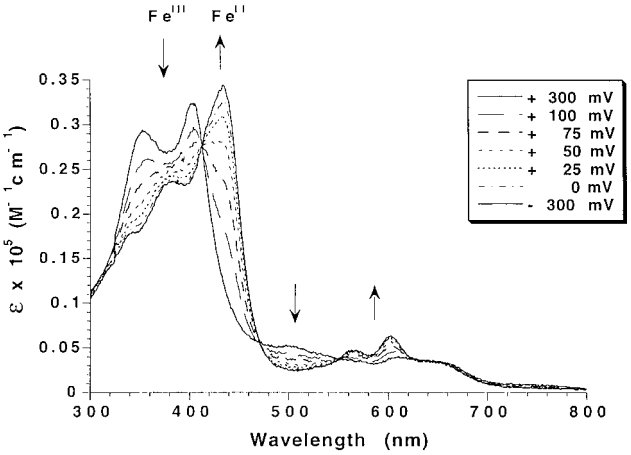

Figure 6. Anodically stepped, potential-dependent electronic spectra obtained for the [5,10,15,20-tetrakis(heptafluoropropyl)porphinato]iron(II) species generated upon bulk reduction of [5,10,15,20-tetrakis(heptafluoropropyl)porphinato]iron·chloride that highlights the $PFe^{II/III}$ redox couple. Experimental conditions: [PFe] = 0.33 mM; [TBAP] = 0.5 M; solvent = CH_2Cl_2.

SCE],[20] indicating that the *meso*-(perfluoroalkyl)porphyrin macrocycle possesses a superior ability to stabilize the ferrous oxidation state with respect to these [5,10,15,20-tetra(substituted)-porphinato]iron·chloride complexes. Table 4 lists comparative cyclic voltammetric data for these species and a number of other relevant PFe complexes; note that the $Fe^{II/III}$ redox couple for $Br_8(C_6F_5)_4PFe{\cdot}Cl$ is 300 mV more positive than that for $(C_3F_7)_4$-$PFe{\cdot}Cl$.

Spectroelectrochemical Experiments. Thin-layer electronic absorption spectral data were taken at controlled potential intervals over a 600-mV domain that spans the $E_{1/2}$ value for the $Fe^{II/III}$ redox process of the $(C_3F_7)_4PFe{\cdot}Cl$ complex; non-isosbestic behavior is observed in the potential-dependent electronic spectra that chronicle the initial PFe^{III}-to-PFe^{II} reduction (Supporting Information). The optical spectra recorded for the controlled-potential oxidation of the $(C_3F_7)_4PFe^{II}$ species generated upon bulk reduction of the $(C_3F_7)PFe{\cdot}Cl$ complex displays isosbestic behavior (Figure 6). Such isosbestic behavior is manifest in all further spectroelectrochemical experiments that repetitively cycle between the anodic and cathodic potentiometric extremes, indicating that the analyte composition is chemically altered by the initial bulk reduction of the sample. The electrogenerated PFe^{III} species observed in the thin-layer spectroelectrochemical experiments possesses an optical spectrum distinct from that of $[(C_3F_7)_4P]Fe{\cdot}Cl$ (Figure 7). The initial nonisosbestic behavior coupled with the modest differences between the electronic spectra observed for the electrochemically generated PFe^{III} species and the $[(C_3F_7)_4P]Fe{\cdot}Cl$ complex suggest that perchlorate−metal interactions play a significant role in the electrochemistry at the high electrolyte concentrations employed in these experiments; such a hypothesis is consistent with a large body of PFe electrochemical data.[21,22] Equations 1−4 summarize the electrode-coupled reactions relevant to potentiometric studies of $[(C_3F_7)_4P]Fe{\cdot}Cl$ when large concentrations of perchlorate ion are present.

$$PFe^{III}Cl + e^- \overset{E_R}{\rightleftharpoons} [PFe^{III}Cl]^- \quad (1)$$

$$[PFe^{III}Cl]^- \rightleftharpoons PFe^{II} + Cl^- \quad (2)$$

$$PFe^{II} + ClO_4^- \rightleftharpoons [PFe^{II}ClO_4]^- \quad (3)$$

$$[PFe^{II}ClO_4]^- \overset{E_O}{\rightleftharpoons} PFe^{III}ClO_4 + e^- \quad (4)$$

Clearly, loss of the halide axial ligand plays a prominent role in the substantial difference in potential between E_{pa} and E_{pc} values for the $Fe^{II/III}$ redox process ($\Delta E_p = 400$ mV) that is observed in the cyclic voltammogram of Figure 5B. Consistent with this, because electrochemically generated PFe^{II} species have drastically reduced affinity for both chloride and perchlorate axial ligands with respect to their PFe^{III} counterparts,[20] and the ratio of $[ClO_4]^-$ to $[Cl]^-$ in these studies is on the order of 10^3, it is not surprising that isosbestic behavior is observed in all cathodically and anodically stepped spectroelectrochemical experiments that follow the initial bulk reduction of (C_3F_7)-$PFe{\cdot}Cl$ (eq 2−3). Analogous experiments executed with $(C_6F_5)_4$-$PFe{\cdot}Cl$ as the analyte give similar results, with the initial cathodically stepped spectroelectrochemical experiment showing

(22) Bottomley, L. A.; Kadish, K. M. *Inorg. Chem.* **1981**, *20*, 1348−1357.

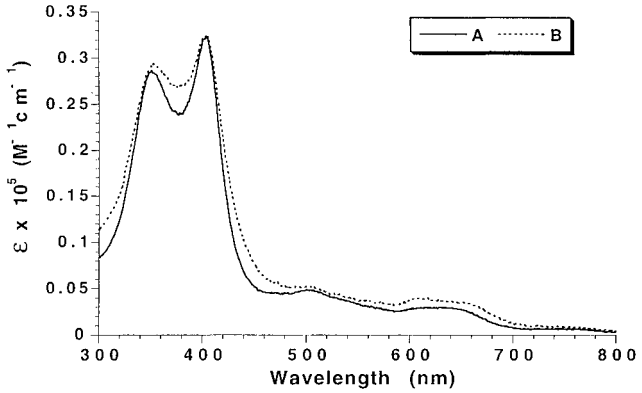

Figure 7. Electronic absorption spectra recorded in CH_2Cl_2 of (A) [5,10,15,20-tetrakis(heptafluoropropyl)porphinato]iron•chloride, and (B) the electrochemically generated [5,10,15,20-tetrakis(heptafluoropropyl)-porphinato]iron(III) species observed in the spectroelectrochemical experiment chronicled in Figure 6.

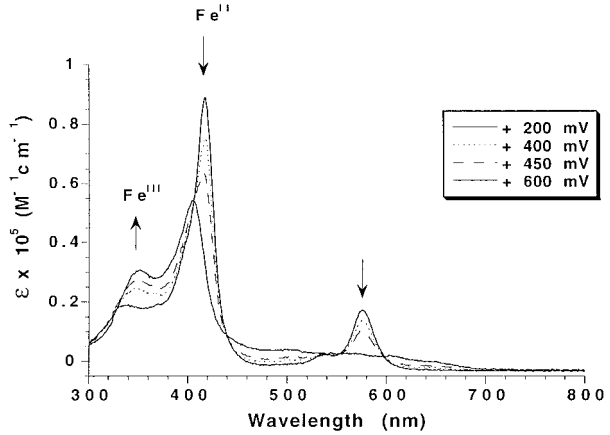

Figure 8. Potential-dependent electronic spectra of [5,10,15,20-tetrakis-(heptafluoropropyl)porphinato]iron•$(py)_2$ highlighting the $PFe^{II/III}$ redox couple. Experimental conditions: [PFe] = 0.12 mM; [TBAP] = 0.5 M; solvent = CH_2Cl_2.

nonisosbestic behavior, while all subsequent bulk oxidations and reductions bear the hallmarks of a single, electrochemically active species in solution whose potential-dependent optical spectra are not influenced by axial ligand dynamics (Supporting Information). Table S1 (Supporting Information) lists the relative concentrations of ferric and ferrous species present for these two PFe systems as a function of potential in these spectroelectrochemical experiments.

Spectroelectrochemical (Figure 8) and cyclic voltammetric (Figure 5A) studies carried out on the low-spin, six-coordinate $(C_3F_7)_4PFe•(py)_2$ reveal an extremely large positive shift in the $Fe^{II/III}$ redox couple [$E_{1/2}$ ($Fe^{II/III}$) = 510 mV] relative to that observed for $(C_3F_7)_4PFe•Cl$ [$E_{1/2}$ ($Fe^{II/III}$) = −10 mV]. Spectroelectrochemical experiments that examine the $Fe^{II/III}$ redox couple of $(C_3F_7)_4PFe•(py)_2$ in the presence of 1.0 M pyridine (see Supporting Information), evince only a modest shift potential [$E_{1/2}$ $Fe^{II/III}$ = 540 mV] relative to that observed for $(C_3F_7)_4PFe•(py)_2$ in the absence of excess axial Lewis base. For comparison, the magnitudes of such axial ligand-dependent potential shifts observed in analogous experiments carried out in benzonitrile involving $(C_6F_5)_4PFe•(py)_2$ in the presence of 1.0 M py [$E_{1/2}$ ($Fe^{II/III}$) = 370 mV] and $(C_6F_5)_4PFe•Cl$ [$E_{1/2}$ ($Fe^{II/III}$) = −110 mV], as well as $Br_8(C_6F_5)_4PFe•Cl$ in the presence of 1.0 M py [$E_{1/2}$ ($Fe^{II/III}$) = +770 mV] and $Br_8(C_6F_5)_4$-$PFe•Cl$ [$E_{1/2}$ ($Fe^{II/III}$) = +290 mV], are noted in Table 4.[23] The $E_{1/2}$ values for the $Fe^{II/III}$ couple are sensitive to the nature of axial ligation and spin state of the metal; note that the potential shift for ferric-to-ferrous reduction in $PFe^{III}•L_2$ complexes relative to their corresponding PFe•Cl species is particularly pronounced in a $(C_3F_7)_4PH_2$ ligand environment ($\Delta E_{1/2}$ = 550 mV). This impressive spin-state dependent potential shift illustrates the particularly effective removal of metal-centered electron density by the macrocycle when the metal is constrained to reside in the porphyrin plane and maximize its electronic interaction with the σ-electron withdrawing, non-π-conjugating *meso* substituents.

Potentiometric Studies of Axial Ligand Binding. Kadish has shown that the relative pyridine binding affinities for PFe^{II} and PFe^{III} species can be evaluated from potentiometric data obtained as a function of exogenous axial ligand concentration;[20,22,23a,b] this relationship between ligand concentration and redox potential can be expressed in a modified version of the Nernst equation.

$$(E_{1/2})_c = (E_{1/2})_s - \frac{0.059}{n}\log\frac{K_{Fe(III)}}{K_{Fe(II)}} - \frac{0.059}{n}\log[L]^{p-q} \quad (5)$$

Here $(E_{1/2})_c$ and $(E_{1/2})_s$ are the half-wave potentials of the bis-axially ligated and axial-ligand-free species, n is the number of electrons transferred, $K_{Fe(III)}$ and $K_{Fe(II)}$ are the formation constants for the $PFe^{II}•L_2$ and $Fe^{III}•L_2$ species, [L] is the concentration of axial ligand, and p and q are the number of ligands respectively bound to the oxidized and reduced species.[20] The magnitude of the potential difference between the $Fe^{II/III}$ redox couples for high- and low-spin Fe^{III} species (determined from the reductive electrochemistry of the PFe•Cl and $[PFe•(py)_2]^+$ complexes) allows the evaluation of the ratio of the Fe^{II} and Fe^{III} axial pyridyl binding constants. As seen in Table 4, the relative preference for maintaining a bis-axially ligated ferrous center is an order of magnitude greater for the $(C_3F_7)_4$-PH_2 macrocycle [$\log(K_{Fe(II)}/K_{Fe(III)}) = 9.2$] with respect to Br_8-$(C_6F_5)_4PH_2$ [$\log(K_{Fe(II)}/K_{Fe(III)}) = 8.2$], $(C_6F_5)_4PH_2$ [$\log(K_{Fe(II)}/K_{Fe(III)}) = 8.0$], and $(C_6H_5)_4PH_2$ [$\log(K_{Fe(II)}/K_{Fe(III)}) = 7.9$] ligands, consistent with the unusually short $Fe-N_{pyridyl}$ bond lengths manifest in the $(C_3F_7)_4PFe•(py)_2$ structure, and the σ-electron withdrawing properties of its *meso* substituents.

In contrast to the extensively studied $(C_6H_5)_4PFe•(L)_2$ systems in which the $Fe^{II/III}$ potential has been observed to shift over a 300-mV range as a function of the exogenous concentration of axial ligand L,[23] the potential at which the $Fe^{II/III}$ redox process occurs for $(C_3F_7)_4PFe•(py)_2$ is seen to be only marginally dependent on pyridine concentration in the cyclic voltammetric experiment; only a 30-mV shift in the $Fe^{II/III}$ potential is observed when exogenous pyridine concentrations are varied over a 10^{-3} to 1.0 M range (Table 4). Because such minor shifts in the $Fe^{II/III}$ potential as a function of added axial ligand may derive solely from modulation of the bulk dielectric or the analyte-localized solvation shell, analyzing these data using eq 5 to calculate redox-dependent differences in formation constants may be inappropriate. These data do indicate, however, that both $(C_3F_7)_4$-PFe^{II} and $(C_3F_7)_4PFe^{III}$ species are essentially bis-axially ligated on the time scale of these cyclic voltammetric experiments and have pyridyl ligand binding constants that are large; this observation is consistent with variable temperature NMR experiments which show that the ferrous porphyrin species

(23) (a) Kadish, K. M.; Bottomley, L. A. *J. Am. Chem. Soc.* **1977**, *99*, 2380−2382. (b) Kadish, K. M.; Bottomley, L. A.; Beroiz, D. *Inorg. Chem.* **1978**, *17*, 1124−1129. (c) Kadish, K. M.; Bottomley, L. A. *Inorg. Chem.* **1980**, *19*, 832−836. (d) Swistak, C.; Mu, X. H.; Kadish, K. M. *Inorg. Chem.* **1987**, *26*, 4360−4366. (e) Kadish, K. M.; Tabard, A.; Lee, W.; Liu, Y. H.; Ratti, C.; Guilard, R. *Inorg. Chem.* **1991**, *30*, 1542−1549.

Table 5. Spectroelectrochemical Data Acquired in the Presence of Exogenous Axial Ligand That Describe the Potential-Dependent Concentration of (Porphinato)iron(II) and -(III) Species for PFe·(pyridine)$_2$ Complexes Based on $(C_3F_7)_4PH_2$, $(C_6F_5)_4PH_2$, and $Br_8(C_6F_5)_4PH_2$ Macrocycles[a]

	% Fe(II)					
potential (V)	$(C_3F_7)_4$PFe·(py)$_2$	$(C_6F_5)_4$PFe·(py)$_2$	$Br_8(C_6F_5)_4$PFe·(py)$_2$	$(C_3F_7)_4$PFe·(py)$_2$ 1.0 M py	$(C_6F_5)_4$PFe·(py)$_2$ 1.0 M py	$Br_8(C_6F_5)_4$PFe·(py)$_2$ 1.0 M py
forward sweep						
−0.10	100	100	100	100	100	100
0.00						
+0.10		85				
+0.20		48				
+0.25		30				
+0.30	94	11	94		99	
+0.40	76	2	76		64	
+0.45	52		26	87	20	
+0.50	18	0	9	57	3	
+0.55	2			22		
+0.60	0		2	0	0	
+0.70			0			
+0.80						64
+0.85						19
+0.90						2
+1.00						0
$E_{1/2}$ for forward sweep	+0.46 V	+0.20 V	+0.45 V	+0.51 V	+0.42 V	+0.82 V

	% Fe(II)					
potential (V)	$(C_3F_7)_4$PFe·(py)$_2$	$(C_6F_5)_4$PFe·(py)$_2$	$Br_8(C_6F_5)_4$PFe·(py)$_2$	$(C_3F_7)_4$PFe·(py)$_2$ 1.0 M py	$(C_6F_5)_4$PFe·(py)$_2$ 1.0 M py	$Br_8(C_6F_5)_4$PFe·(py)$_2$ 1.0 M py
reverse sweep						
+1.00	0	0	0	0	0	0
+0.85						28
+0.80						64
+0.70						100
+0.60						
+0.55				14		
+0.50	19		17	50	2	
+0.45			48	82	18	
+0.40	49		74		61	
+0.30	64	4	94		99	
+0.20	72	15				
+0.15		31				
+0.10	89	62				
0.00	99	96	100	100	100	
−0.10	100	100				
$E_{1/2}$ for reverse sweep	+0.39 V	+0.12 V	+0.45 V	+0.50 V	+0.42 V	+0.82 V

[a] The spectroelectrochemical cell was charged initially with the (porphinato)iron·(pyridine)$_2$ complex. Experimental conditions: [PFe] = 0.14 mM; [TBAP] = 0.5 M; solvent = CH_2Cl_2; reference electrode = SCE. Electronic spectra were recorded when the current passed at the working electrode ceased at each specified potential.

present in benzene-d_6 solution that contains no added pyridine at room temperature is predominantly the six-coordinate $(C_3F_7)_4$PFe·(L)$_2$ complex.[1c,d]

These differences in axial ligand binding affinity for the ferric and ferrous derivatives of the $(C_3F_7)_4PH_2$, $(C_6F_5)_4PH_2$, and $Br_8(C_6F_5)_4PH_2$ ligand systems are also evident in Table 5, which displays the relative concentrations of PFe^{II} and PFe^{III} species present as a function of potential evaluated from our spectroelectrochemical experiments for both the cathodically stepped ferric-to-ferrous redox processes and the anodically stepped ferrous-to-ferric conversions. The minimal dependence of the PFe$^{II/III}$ potential upon exogenous pyridine for the $(C_3F_7)_4$PFe·(py)$_2$ complex stands in sharp contrast to the electrochemical data obtained for $(C_6F_5)_4$PFe·(py)$_2$ and $Br_8(C_6F_5)_4$PFe·(py)$_2$ (Supporting Information; Table 5). As highlighted in Table 5, $Br_8(C_6F_5)_4$PFe·(py)$_2$, $(C_6F_5)_4$PFe·(py)$_2$, and $(C_3F_7)_4$PFe·(py)$_2$ exhibit potentiometric shifts in their Fe$^{II/III}$ $E_{1/2}$ values of 370, 220, and 50 mV, respectively, when the concentration of the exogenous pyridine is increased from 0.0 to 1.0 M in anodically stepped spectroelectrochemical experiments involving their PFe^{II}L$_2$ derivatives.[24] While added axial ligand stabilizes both PFe^{II} and PFe^{III} species, positive shifts in the Fe$^{II/III}$ redox potential with augmented axial ligand concentration have been shown by Kadish to correlate with preferential stabilization of the ferrous oxidation state for bis-axially ligated structures.[20,22,23] The large pyridine concentration dependent potentiometric shifts observed for comparably electron-deficient $Br_8(C_6F_5)_4$PFe species derive from the π-conjugating nature of its macrocycle-appended substituents[1a,b] and the fact that $Br_8(C_6F_5)_4$PFe·(py)$_2$ possesses a substantial saddle distortion,[24] which likely diminishes the magnitude of the PFe·L$_2$ formation constants for both

(24) The Fe$^{II/III}$ redox potential evaluated from spectroelectrochemical data obtained for [$Br_8(C_6F_5)_4$P]Fe^{II}·(py)$_2$] in 0.5 M TBAP in CH_2Cl_2 in the absence of any added axial ligand did not correspond to that derived from previously reported cyclic voltammetric data; performing spectroelectrochemical experiments in the presence of 1.0 M pyridine gave an Fe$^{II/III}$ redox potential of 820 mV vs SCE, consistent with earlier work. See: Grinstaff, M. W.; Hill, M. G.; Birnbaum, E. R.; Schaefer, W. P.; Labinger, J. A.; Gray, H. B. *Inorg. Chem.* **1995**, *34*, 4896−4902.

Scheme 1. Summaries of PFe Cathodic Electrochemistry Determined from Cyclic Voltammetric Measurements[a]

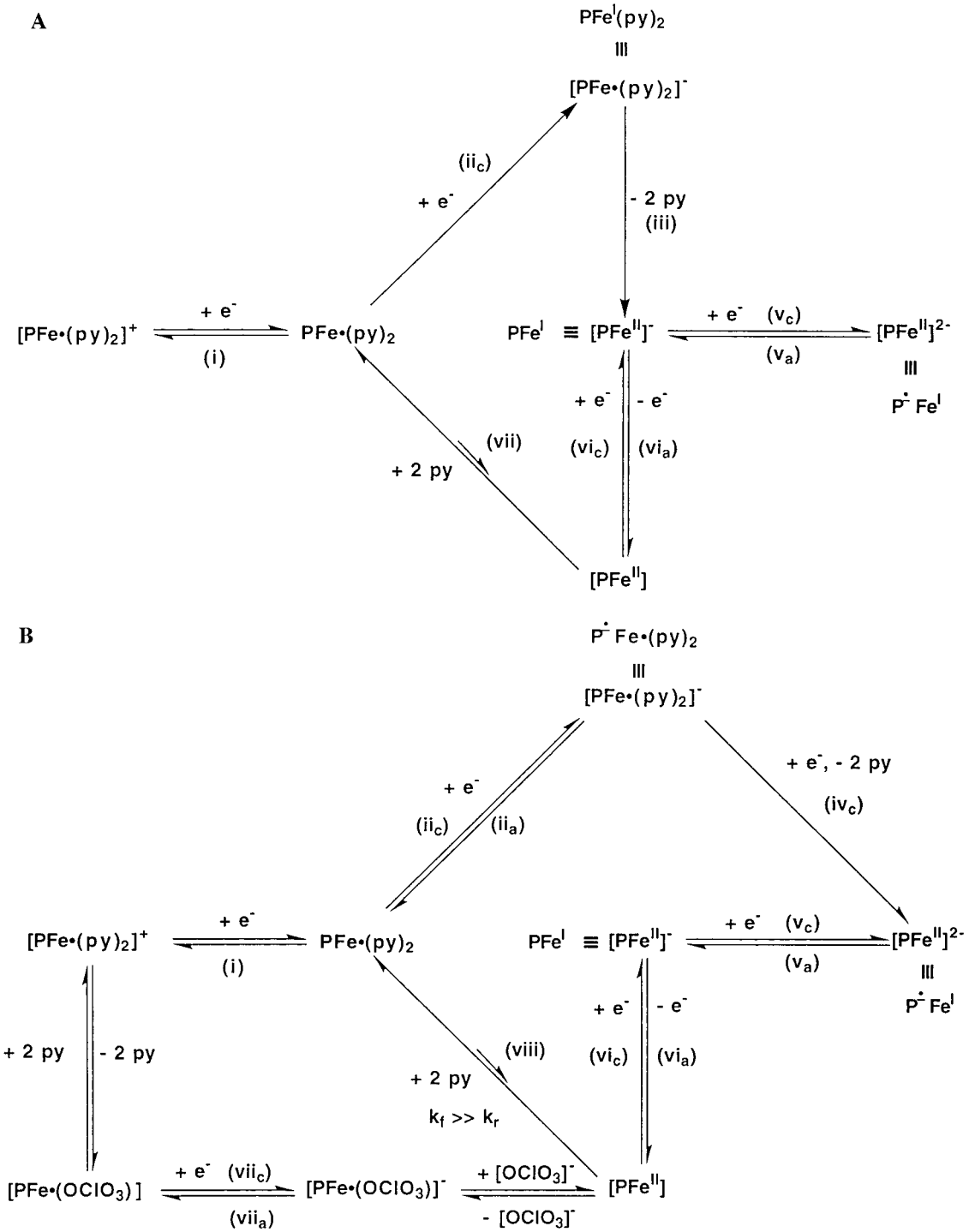

[a] (A) for $(C_6H_5)_4PFe\cdot(py)_2$ and related species, the initial reductive process generates a PFe^I compound; this mechanistic model has been previously described by Kadish.[20] (B) For $(C_3F_7)_4PFe\cdot(py)_2$, the initial reductive process generates a macrocycle-localized radical anion.

the ferric and ferrous oxidation states relative to respective $[(C_3F_7)_4PFe\cdot(py)_2]^+$ and $(C_3F_7)_4PFe\cdot(py)_2$ species (vide infra).

Cathodic Electrochemistry of $(C_3F_7)_4PFe^{II}$ Species. The reductive electrochemistry of $PFe\cdot(L)_2$ complexes has been extensively studied.[20,21,23,25] Mechanistic work investigating $(C_6H_5)_4PFe\cdot(py)_2$ and related systems shows that the first electrode-coupled reduction of such species produces a radical anion with significant metal d_{z^2} character; rapid loss of both axial ligands ensues, producing a species commonly classified as a PFe^I complex. A second reductive process gives rise to a porphyrin radical anion, $[PFe^I]^{\bullet-}$; this species can be oxidized in two chemically reversible one-electron (1e) steps to produce a four-coordinate PFe^{II} species. Furthermore, the cyclic voltammetric responses corresponding to the oxidation of the ferrous porphyrin are often complicated by axial ligand reassociation kinetics;[20,23] this mechanistic picture is summarized in Scheme 1A.

Figure 9A and B displays cyclic voltammetric responses obtained for $(C_3F_7)PFe\cdot(py)_2$ over the 1.00 to −1.40 V potential domain as a function of exogenous axial ligand concentration.

(25) Lexa, D.; Momenteau, M.; Mispelter, J.; Lhoste, J. M. *Bioelectrochem. Bioenerg.* **1974**, *1*, 108−117.

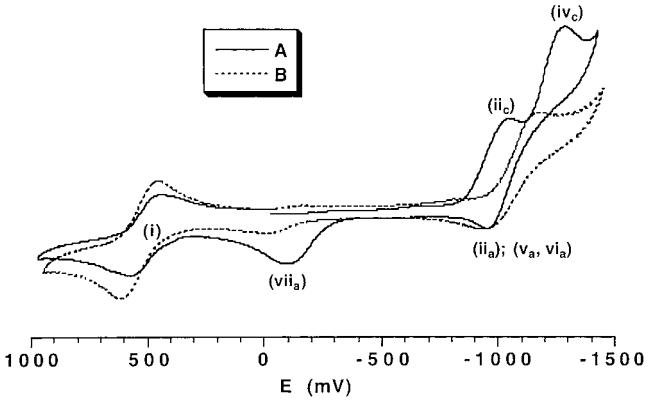

Figure 9. Cyclic voltammetric responses obtained for [5,10,15,20-tetrakis(heptafluoropropyl)porphinato]iron•(py)$_2$ in (A) neat benzonitrile and (B) benzonitrile with 1.0 M pyridine. Experimental conditions: [PFe] = 5 mM; [TBAP] = 0.1 M; $E_{initial} = E_{final} = 0.00$ V; switching potentials (E_{sw}): $E_{sw1} = -1.40$ V, $E_{sw2} = 1.0$ V; scan rate = 500 mV/s.

In these experiments, the potential was first swept cathodically from an initial potential (E_i) of 0.00 V to −1.40V; at the reductive switching potential ($E_{sw1} = -1.40$ V), the potential was swept to the anodic switching potential ($E_{sw2} = 1.0$ V) and then terminated at the final potential ($E_f = 0.00$ V). Figure 9A shows the cyclic voltammetric response obtained for the $(C_3F_7)_4$-PFe•$(py)_2$ complex in the initial sweep through this potential window; one electron cathodic processes ii_c ($E_{pc} = -1050$ mV) and iv_c ($E_{pc} = -1290$ mV) are observed, along with anodic processes ii_a ($E_{pa} = -950$ mV) and vii_a ($E_{pa} = -100$ mV), and the $Fe^{II/III}$ redox couple ($E_{1/2} = +510$ mV).

Cyclic voltammetric experiments carried under conditions identical to that described for Figure 9A except that the cathodic switching potential was set at −1.1 V show redox processes ii_c, ii_a, i_a, and i_c; anodic process vii_a is absent under these conditions (data not shown). The cyclic voltammetric response obtained for an independently synthesized $(C_3F_7)_4$PFe•$OClO_3$ sample suggests that redox process vii_a corresponds to the anodic component of the $[(C_3F_7)_4PFe•OClO_3]^{-/0}$ couple. Furthermore, augmenting exogenous pyridine levels underscores the potentiometric sensitivity of cathodic process iv_c to increased levels of axial ligand in solution; at an exogenous pyridine concentration of 1.0 M, cathodic process iv_c shifts to the edge of the cathodic window accessible for such a benzonitrile solution and the current response recorded at potential vii_a is essentially quenched (Figure 9B).

It is important to note that in contrast, initial cathodic process ii_c is much less sensitive to exogenous pyridine concentration and is shifted by only −120 mV upon addition of 1.0 M pyridine; a potential shift of this magnitude likely reflects that small differences in axial ligand binding affinity exist between $[(C_3F_7)_4PFe•(py)_2]^{•-}$ and $(C_3F_7)_4PFe•(py)_2$. The −120 mV cathodic shift observed upon the addition of 1.0 M pyridine for process ii_c is modest in comparison to that observed for cathodic process iv_c, which is shifted by over −350 mV in the presence 1.0 M pyridine. Such an observation is consistent with the formation of a formal $P^{•-}Fe^{I}$ compound; congruent with this, it has been reported that the cathodic potential that generates the PFe^{I} state for $(C_6H_5)_4PFe•(py)_2$ typically shifts by ∼ −250 mV in the presence of 1.0 M pyridine.[23c]

In contrast to previous mechanistic work that examined the cathodic electrode-coupled reactions of conventional $PFe^{II}•(L)_2$ species (Scheme 1A), these cyclic voltammetric experiments carried out on $[(C_3F_7)_4PFe•(py)_2]$ are consistent with the general mechanistic description outlined in Scheme 1B. The initial cathodic redox process produces a macrocycle-localized radical anion, which maintains high binding affinity for its axial ligands. The electrode-coupled reduction of this $[(C_3F_7)_4PFe•(py)_2]^{•-}$ species corresponds to an EC process (heterogeneous electron transfer followed by axial ligand loss), giving rise to four-coordinate $[(C_3F_7)_4PFe]^{2-}$, which is formulated as a $P^{•-}Fe^{I}$ compound. The production of a significant quantity of $[(C_3F_7)_4$-$PFe^{III}•OClO_3]^-$ at the electrode surface as evinced by anodic process vii_a implies either the existence of redox processes v_a and vi_a (Scheme 1B) to produce a PFe^{II} complex void of axial pyridyl groups or that the transiently generated $[(C_3F_7)_4PFe•$-$(py)_2]^{2-}$ species decomposes via loss of two pyridyl radical anions. Whatever the nature of the electrode and electrode-coupled chemical processes that follow the reduction of macrocycle-localized radical anion species $[(C_3F_7)_4PFe•(py)_2]^{•-}$, they were not investigated further due to their irreversible nature. This electrochemical data is consistent with the previously demonstrated extensive stabilization of the e_g-symmetric LUMO in $(C_3F_7)_4PH_2$ macrocycles[1a,b] and defines an unusual case in which macrocycle reduction precedes metal reduction for $PFe^{II}•$-$(L)_2$ complexes. These data suggests that modulating the nature of axial ligation in $(C_3F_7)_4PFe•(L)_2$ complexes should allow considerable control over the relative stabilities of the empty iron d_{z^2} and porphyrin e_g orbitals and the corresponding chemistry that occurs upon the 1e reduction of such compounds.

Evaluating the magnitude of the $PFe^{II/I}$ redox potential for a PFe^{II} species in the presence and absence of 1.0 M axial ligand, and applying a modified version of eq 5 permits the direct calculation of the formation constants ($K_{Fe(II)}$) for the $PFe^{II}•L_2$ species (eq 6).[20]

$$\log K_{Fe(II)} = \frac{(E_{1/2})_c - (E_{1/2})_{s'}}{0.059\ V} \qquad (6)$$

Here $(E_{1/2})_{c'}$ and $(E_{1/2})_{s'}$ are the reductive half-wave potentials of the bis-axially ligated and axial-ligand-free PFe^{II} species. For the $(C_3F_7)_4PFe$ system, the relevant redox potential that produces an Fe^{I} species corresponds to the $[PFe]^{2-/1-}$ couple; unfortunately, evaluation of the potential for the $[(C_3F_7)_4PFe•(py)_2]^{2-/1-}$ couple in the presence of excess axial ligand is precluded by the cathodic window accessible for benzonitrile solutions containing 1.0 M pyridine. An estimation of the magnitude of this binding constant can be calculated using the cathodic solvent breakdown potential as the upper limit for $(E_{1/2})_{c'}$, giving log $K_{Fe(II)} \geq 4.7$.[26]

From the pyridine concentration-dependent potentiometric shifts of the $PFe^{II/III}$ redox couple and the electrochemical experiments examining the $PFe^{I/II}$ redox process, log $K_{Fe(III)}$ values can be calculated. Table 4 lists log $K_{Fe(III)}/K_{Fe(II)}$ and log $K_{Fe(II)}$ values; from these and related data,[1d] it is evident that relative to the $[Br_8(C_6F_5)PFe]^+$, $[(C_3F_7)_4PFe]^+$ possesses a significantly larger formation constant for its corresponding $PFe^{III}•(py)_2$ complex.

EPR Spectroscopy of $[(C_3F_7)_4PFe•(py)_2]^+$. Because PFe^{III} complexes of electron-deficient porphyrin macrocycles are prone to autoreduction when exposed to large excesses of exogenous pyridyl compounds,[21c,27] $(C_3F_7)_4PFe•Cl$ was reacted with 2 equiv of pyridine in CH_2Cl_2 at ambient temperature and then frozen

(26) Variable temperature NMR data described elsewhere have been utilized to assess the magnitude of log $K_{Fe(II)}$ for $(C_3F_7)_4PFe$;[1d] these data show that the formation constant for pyridine binding is substantial for $(C_3F_7)_4PFe$, and exceeds by several orders of magnitude that elucidated for $(C_6F_5)_4PFe$ using electrochemical methods (Table 4).

(27) Balch, A. L.; Noll, B. C.; Olmstead, M. M.; Phillips, S. L. *Inorg. Chem.* **1996**, *35*, 6495−6506.

Table 6. EPR Parameters of Low-Spin PFe^{III} Complexes

PFe^{III} unit	axial ligands	g_x	g_y	g_z	Σg^2	Δ/λ[a]	mixing coefficients (*a*,*b*,*c*)	% d_{xy}[a]	reference
$(C_3F_7)_4PFe$	pyridine	2.07	2.07	1.99	12.53	−26.4	0.019, 0.019, 0.998	99	this work
$(C_6H_5)_4PFe$	*t*-BuNC[c]	2.19	2.19	1.93	13.36	−8.33	0.063, 0.063, 0.990	98	28e
OEPFe[b]	*t*-BuNC	2.28	2.28	1.83	13.74	−5.47	0.096, 0.096, 0.976	95	28e
$(C_6H_5)_4PFe$	4-CN-py[d]	2.62	2.62	0.92	14.57	−1.72	0.289, 0.289, 0.891	82.5	13e
$(C_6H_5)_4PFe$	pyridine	1.2	1.7[e]	3.4	16.0	+6.53	0.913, 0.394, 0.090	0.8	28c

[a] Tetragonality parameter (Δ/λ), mixing coefficients (*a*, *b*, *c*), and $\%d_{xy}$ character were calculated using the Taylor model for a "proper axis system" with $g_x = -|g_x|$, $g_y = +|g_y|$, $g_z = -|g_z|$.[28a,e,f] [b] OEP = 2,3,7,8,12,13,17,18-octaethylporphyrin. [c] *t*-BuNC = *tert*-butylisocyanide. [d] 4-CN-py = 4-cyanopyridine. [e] Estimated; see ref 28c.

Figure 10. EPR spectrum of [5,10,15,20-tetrakis(heptafluoropropyl)-porphinato]iron·chloride with 2 equiv of added pyridine at 10 K. A minor free radical contribution that derives from the pyridine-induced autoreduction of (porphinato)iron(III) has been subtracted out. Inset: spectral simulation obtained using the Bruker SimFonia simulation package. Simulation parameters: $g_x = 1.97$, $g_y = 2.007$, $g_z = 2.072$, width = 55 mT.

at 78 K. The EPR spectrum of low-spin $[(C_3F_7)_4PFe\cdot(py)_2]^+$ $[Cl]^-$ is shown in Figure 10; Table 6 lists relevant EPR spectroscopic parameters determined for this complex as well as those for benchmark low-spin ferric heme complexes. The magnitude of the EPR *g* values gives insight into the electronic configuration at the low spin d^5-iron center; most naturally occurring low spin ferriheme complexes and PFe model systems possess a $(d_{xy})^2(d_{xz},d_{yz})^3$ ground state and thus evince a rhombic EPR spectrum which derives from the loss of degeneracy in the highest occupied d_{xz} and d_{yz} orbitals when these species are exposed to an external magnetic field. The characteristic features of low spin PFe^{III} complexes featuring this electronic state are typified by $[(C_6H_5)_4Fe\cdot(py)_2]^+$ (Table 6);[28] for such species, the tetragonality parameter Δ/λ, which reflects the relative energy between the d_{xy} and d_{xz}, d_{yz}, is a positive value, and $\Sigma g^2 = 16$. Using the Taylor model,[28a] the mixing coefficients for the d_{xz}, d_{yz}, and d_{xy} wave functions can be calculated; the resulting unpaired spin density residing in d_{xy} for $[(C_6H_5)_4Fe\cdot(py)_2]^+$ is less than 1% (Table 6).

Recently, Scheidt, Walker, and Debrunner have explored a class of low spin PFe^{III} complexes that possesses a large degree of $(d_{xz},d_{yz})^4(d_{xy})^1$ character; these $PFe^{III}\cdot L_2$ systems feature conventional porphyrin macrocycles [$(C_6H_5)_4PH_2$ or 2,3,7,8,-12,13,17,18,-octaethylporphyrin, $(\beta\text{-}C_2H_5)_8PH_2$)] and electron-withdrawing pyridine- or isocyanide-based axial ligands.[13e,28e] The EPR spectra of these complexes show axial symmetry with tetragonality parameters ranging from −1.72 to −8.33; as seen in Table 6, these species exhibit negative values for Δ/λ indicating that the d_{xz} and d_{yz} orbitals are lower in energy[28a] than d_{xy}. Because the rhombic splitting of the d_{xz} and d_{yz} observed normally for hemes possessing a $(d_{xy})^2(d_{xz},d_{yz})^3$ ground state is completely quenched in an axially symmetric system (i.e., a $(d_{xz}\ d_{yz})^4(d_{xy})^1$ electronic configuration), the spin−orbit interactions can be directly correlated with the energy of the d_{xy} orbital relative to the degenerate d_{xz}, d_{yz} set. The magnitude of the tetragonality parameter reflects this energetic difference; as this parameter approaches negative infinity, the degree of spin−orbit coupling becomes negligible, and an isotropic EPR signal with $\Sigma g^2 = 12$ is manifest. Note that $[(C_3F_7)_4PFe\cdot(py)_2]^+$ evinces the expected EPR parameters for an axial system with very little spin−orbit coupling ($\Sigma g^2 = 12.53$; $\Delta/\lambda = -26.4$) and manifests by far the largest energetic difference between the d_{xy} and d_{xz},d_{yz} orbitals yet observed for a $PFe^{III}\cdot L_2$ complex (Figure 10, Table 6). Given that the $(C_6H_5)_4Fe^{III}\cdot$(*tert*-butyl isocyanide)$_2$ complex ($\Sigma g^2 = 13.49$, $\Delta/\lambda = -8.33$, d_{xy} character (HOMO) = 98%) has served as the archetype for $(d_{xz},d_{yz})^4$ $(d_{xy})^1$ ground state, $[(C_3F_7)_4PFe\cdot(py)_2]^+$ not only sets a new standard for efficient quenching of orbital angular momentum in a low-spin d^5 (porphinato)metal system; it complements this earlier work by demonstrating that such electronic configurations can be accessed through electronic modulation of the porphyrin macrocycle.

(28) (a) Taylor, C. P. S. *Biochim. Biophys. Acta* **1977**, *491*, 137−149. (b) Reed, C. A.; Mashiko, T.; Bentley, S. P.; Kastner, M. E.; Scheidt, W. R.; Spartalian, K.; Lang, G. *J. Am. Chem. Soc.* **1979**, *101*, 2948−2958. (c) Walker, F. A.; Reis, D.; Balke, V. L. *J. Am. Chem. Soc.* **1984**, *106*, 6888−6898. (d) Walker, F. A.; Huynh, B. H.; Scheidt, W. R.; Osvath, S. R. *J. Am. Chem. Soc.* **1986**, *108*, 5288−5297. (e) Walker, F. A.; Nasri, H.; Turowska-Tyrk, I.; Mohanrao, K.; Watson, C. T.; Shokhirev, N. V.; Debrunner, P. G.; Scheidt, W. R. *J. Am. Chem. Soc.* **1996**, *118*, 12109−12118.

Summary and Conclusions

The structural, spectroscopic, and potentiometric data reported herein for these $(C_3F_7)_4PFe$ species evince a number of unprecedented properties with respect to other previously characterized PFe complexes. (i) The single-crystal X-ray data show that $(C_3F_7)_4PFe\cdot(py)_2$ is the only example of a ferrous porphyrin that exhibits all of the signature metrical parameters that delimit ferric porphyrin complexes; hallmarks of this structure include extremely short $Fe-N_{pyrrolyl}$ and $Fe-N_{pyridyl}$ bond lengths, mutually staggered pyridine ligands, and an extensive macrocycle S_4 ruffling distortion. No other low-spin $PFe^{II}\cdot L_2$ species are known to be stabilized by such severe porphyrin ring-ruffling. These unusual structural features imply that the d_{xy} and d_{xz},d_{yz} energy levels are uniquely inverted in $(C_3F_7)_4PFe\cdot(py)_2$ with respect to other $PFe^{II}\cdot L_2$ compounds. (ii) Potentiometric studies reveal that the $E_{1/2}$ value for the $Fe^{II/III}$ redox couple for $(C_3F_7)_4PFe\cdot(py)_2$ is remarkable in that it is shifted anodically 550 mV relative to that observed $(C_3F_7)_4PFe\cdot Cl$; metal-centered redox processes are thus seen to be extraordinarily sensitive to the nature of axial ligation and metal spin state in a $(C_3F_7)_4PH_2$ ligand environment and demonstrate that the $(R_f)_4PH_2$ ligand will manifest the most impressive redox modulation when the metal atom is constrained to reside in the porphyrin plane and maximize its electronic interaction with the σ-electron withdrawing, non-π-conjugating meso substituents. (iii) $[(C_3F_7)_4PFe\cdot(py)_2]^{0/+}$ possesses a greater affinity for axial pyridyl ligands than has been elucidated for the analogous oxidation states of other classes of PFe complexes; furthermore, the ratio of the PFe^{II}/PFe^{III} binding constants is an order of magnitude greater than that observed in the benchmark electron-deficient PFe systems $[(C_6F_5)_4PFe^{II}\cdot(py)_2]^{0/+}$ and $[Br_8(C_6F_5)_4PFe^{II}\cdot(py)_2]^{0/+}$. (iv) The cathodic electrochemistry of $(C_3F_7)_4PFe\cdot(py)_2$ differs from that previously explicated for $(C_6H_5)_4PFe\cdot(py)_2$ complexes, and suggests that the first reduction of $(C_3F_7)_4PFe\cdot(py)_2$ produces a largely macrocycle-localized radical anion. (v) EPR spectroscopic studies of $[(C_3F_7)_4PFe\cdot(py)_2]^+$ reveal a $(d_{xz},d_{yz})^4$ $(d_{xy})^1$ ground electronic state ($\Delta/\lambda = -26.4$ and $\sum g^2 = 12.53$); this system possesses the purest d_{xy} HOMO yet observed for a ferric porphyrin complex. Importantly, this study demonstrates that such PFe d electron configurations are stable in the presence of strong Lewis bases and can be readily accessed via electronic modulation of the macrocycle.

Finally, this work shows that the electronic properties of $(R_f)_4PH_2$ macrocycles endow their corresponding iron complexes with a number of properties that may have important ramifications for catalyst design. For example, because electrochemical experiments indicate that macrocycle reduction *precedes* metal reduction for $(C_3F_7)_4PFe\cdot(py)_2$, it suggests that this porphyrin structural motif may find utility in facilitating electrocatalytic reduction of small molecules at driving forces close to their thermodynamic potential via nonradical intermediates; one electron can presumably be stored initially on the tetradentate ligand of $[(C_3F_7)_4PFe\cdot(L)(L')]^{\bullet-}$ complexes and hence thereby suppress axial ligand dissociation prior to the input of the second, metal-localized reducing equivalent that launches axial ligand reduction. Likewise, because the $(C_3F_7)_4PFe\cdot(py)_2$ structure resembles that of a conventional ferric porphyrin, it suggests that related ligand environments could be relevant to the further development of biomimetic catalytic cycles that exploit high-valent (porphinato)metal intermediates in atom transfer reactions.[29]

Acknowledgment. M.J.T. is indebted to the National Science Foundation (CHE93-57130) and the Office of Naval Research (N0014-98-0187) for financial support and gratefully acknowledges the Searle Scholars Program (Chicago Community Trust), the Arnold and Mabel Beckman Foundation, and E. I. du Pont de Nemours for Young Investigator Awards, as well as the Alfred P. Sloan and Camille and Henry Dreyfus Foundations for research fellowships. The authors thank Drs. James G. Goll and Paul J. Angiolillo for helpful discussions and Dr. George T. Furst for experimental assistance with a number of the NMR experiments.

Supporting Information Available: Tables of crystal data, structure solution and refinement, atomic coordinates, bond lengths and angles, and anisotropic thermal parameters for 5,10,15,20-tetrakis(heptafluoropropyl)porphinato]iron(II)·(pyridine)$_2$ are available (X-ray crystallographic file; CIF format) along with additional optical and electrochemical data (PDF). This material is available free of charge via the Internet at http://pubs.acs.org.

JA9816741

(29) (a) Groves, J. T. *J. Chem. Educ.* **1985**, *62*, 928−931. (b) Mansuy, D. *Pure Appl. Chem.* **1987**, *59*, 759−770. (c) Ellis, P. E., Jr.; Lyons, J. E. *Coord. Chem. Rev.* **1990**, *105*, 181−193. (d) Collman, J. P.; Zhang, X.; Lee, V. J.; Uffelman, E. S.; Brauman, J. I. *Science* **1993**, *261*, 1404−1411.